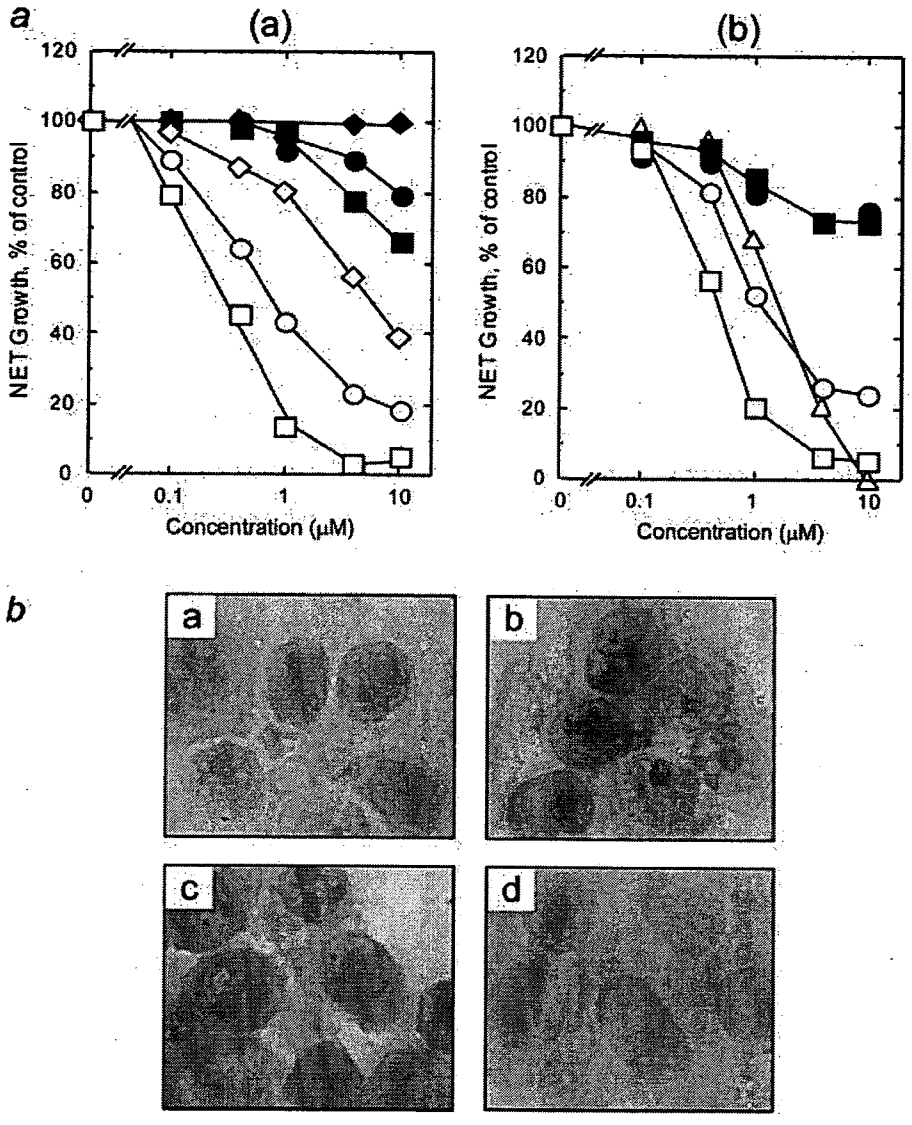

FIGURE 2 – Growth of PC-3 cells in the presence of *p*-alkylaminophenols and 4-hydroxyphenyl analogs and apoptotic cells with fragmented chromatin induced by *p*-DDAP and 4-HPR (*a*-a) PC-3 cells (5×10^4 cells/ml) were grown with various concentrations of *p*-alkylaminophenols exhibiting various alkyl chain length [*p*-DDAP (□), *p*-DAP (○), *p*-OAP (□), *p*-HAP (■), *p*-BAP (●) and *p*-MAP (□)] in a medium containing 10% FBS. Growth was measured at 54 hr as described under "Material and methods." (*a*-b) PC-3 cells (5×10^4 cells/ml) were grown with various concentrations of *p*-alkylaminophenols (*p*-DDAP (□) and *p*-DAP (○)), 4-hydroxyphenyl analogs (4-HPDD (■) and 4-HPD (●) and 4-HPR (□)) in medium containing 10% FBS. Growth was measured at 48 hr as described under "Material and methods." Each point is the mean of at least 4 measurements. The SD of each point was ≤8% of the mean. (*b*) PC-3 cells (5×10^4 cells/ml) were grown in the presence of DMSO (a), *p*-DDAP (b), 4-HPR (c) and 4-HPDD (d) at the concentration of 4 μM in medium containing 10% FBS for 17 hr, and then fixed and stained with Wright-Giemsa staining solution. Morphological changes were visualized by light microscopy.

At a concentration of 4 μM, cell growth was inhibited ~0.8% by *p*-MAP (C_1), ~7.5% by *p*-BAP (C_4), ~21.9% by *p*-HAP (C_6), ~44.2% by *p*-OAP (C_8), ~76.5% by *p*-DAP (C_{10}) and ~96.7% by *p*-DDAP (C_{12}). Thus, among the 6 *p*-alkylaminophenols *p*-DDAP was the most potent anticancer agent against the PC-3 human prostate cancer cell line in addition to the DU-145 cells.

Next, we investigated the effects on PC-3 cell growth of the *p*-alkylaminophenols, *p*-DDAP having a dodecyl residue and *p*-DAP having a decyl residue when compared with the *p*-acyl analogs, 4-HPDD having a dodecanoyl residue (Fig. 1, bottom) and 4-HPD having a decanoyl residue and 4-HPR. Growth of PC-3 cells in the presence of various concentrations of these aminophenols was inhibited in a dose-dependent fashion. At low concentrations in the range of 0.1–1 μM, *p*-DDAP and *p*-DAP inhibited cell growth more potently than 4-HPR (Fig. 2*a*-b). In contrast, 4-HPDD and 4-HPD were poor inhibitors of cell growth independent of side-chain length. At a concentration of 1 μM, *p*-DDAP (~79.6% inhibition) was more potent than *p*-DAP (~47.9% inhibition), 4-HPR (~31.9% inhibition), 4-HPDD and 4-HPD (~16.5% inhibition) (Fig. 2*a*-b). Elongation of the alkyl chain attached to the aminophenol residue in *p*-DDAP and *p*-DAP increased antiproliferative activities, while elongation of the acyl chain attached to the aminophenol residue in 4-HPDD and 4-HPD had almost no effect. Inhibition of cell growth by *p*-alkylaminophenols was ~10–20 fold greater than by *p*-acylaminophenols having acyl residues instead of alkyl chains.

These results indicate that PC-3 cell growth is suppressed by *p*-DDAP more strongly than by other aminophenols and 4-HPR, and that the inhibition of cell growth by these compounds including *p*-DDAP can not be attributed to cell necrosis. In addition, the hydrophobic properties of a dodecyl residue linked to the aminophenol may be significant for antitumor potency with mild effects at low concentrations.

Morphology of PC-3 cells treated with p-DDAP, 4-HPDD and 4-HPR

PC-3 cells were grown in the presence of 4 μM of 2 aminophenol analogs, *p*-DDAP and 4-HPDD, with 4-HPR being used as an internal standard for determining cell morphology (Fig. 1). As shown in Figure 2*b*, PC-3 cells treated with 4-HPDD exhibited enlarged nuclei without any chromosome condensation (Fig. 2*b*-d)

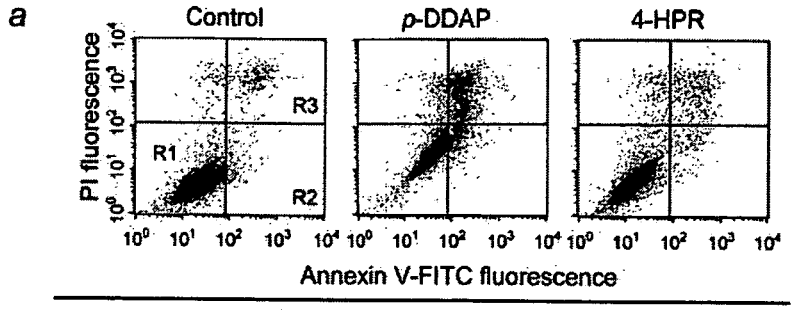

Treatment	R1 Viable cells (Annexin V-, PI-)	R2 Early apoptotic cells (Annexin V+, PI-)	R3 Terminal apoptotic or necrotic cells (Annexin V+, PI+)
Control	92.8%	2.7%	3.2%
p-DDAP	54.8%	9.5%	29.4%
4-HPR	87.0%	3.5%	7.4%

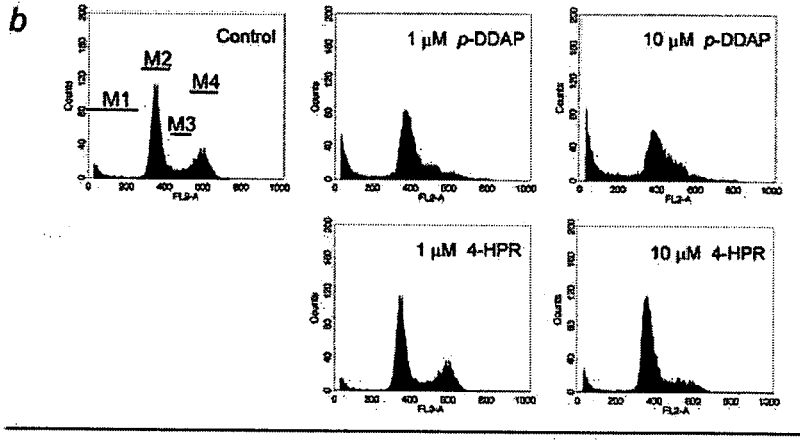

Treatment		% of cell population in M1: sub-G_1	M2: G_0/G_1	M3: S	M4: G_2/M
Control	-	6.36±0.37	64.98±0.76	11.50±0.39	23.51±0.91
p-DDAP	1 μM	19.65±0.74***	68.46±0.43	20.08±0.34***	11.46±0.17
	10 μM	31.18±0.26***	58.86±0.49	30.38±0.36***	10.76±0.23
4-HPR	1 μM	5.53±0.22	64.91±0.90	10.50±0.25	24.59±0.80
	10 μM	8.49±0.10**	75.54±0.20**	13.08±0.22	11.38±0.18

**$p < 0.001$, ***$p < 0.0001$

FIGURE 3 – Flow cytometry assessment of apoptotic cells and cell cycle distribution in PC-3 cells induced by *p*-DDAP and 4-HPR. (*a*) PC-3 cells (5×10^4 cells/ml) were treated with DMSO (Control), 4 μM *p*-DDAP and 4 μM 4-HPR for 48 hr and stained with annexin V and propidium iodide (PI). The dot plots showed representative FACS cytograms of stained cells. Viable cells were in the lower left-hand quadrant (annexin V negative, PI-negative: R1). Early apoptotic cells were in the lower right-hand quadrant (annexin V positive, PI-negative: R2). Terminal apoptotic or necrotic cells were in the upper right-hand quadrant (annexin V-positive, PI-positive: R3). Sizes of subpopulations were given as percentage of total populations and summarized under cytograms. (*b*) PC-3 cells (5×10^4 cells/ml) were treated with DMSO (Control), *p*-DDAP (1 μM, 10 μM) and 4-HPR (1 μM, 10 μM) for 48 hr. Cells were collected and processed for analysis of cell cycle distribution as described under "Material and methods." The histogram showed representative examples of cell cycle analysis by flow cytometry after PI staining. M1 corresponds to the apoptotic sub-G_1 peak, M2 to G_0/G_1, M3 to S-phase and M4 to G_2/M. Sizes of subpopulations were given as the percentage of total populations and summarized under cytograms of cell cycle. Results represent the mean of ± SD of each group. **$p < 0.01$ and ***$p < 0.001$ *versus* control compared by Student's *t*-test.

similar to control cells treated with DMSO (Fig. 2*b*-a). In contrast, chromosome condensations were seen in the nuclei of PC-3 cells treated with *p*-DDAP and 4-HPR (Figs. 2*b*-b and 2*b*-c). These results suggested that *p*-DDAP may induce apoptosis of PC-3 cells.

Apoptosis of PC-3 cells treated with p-DDAP and 4-HPR

Next, we examined the level and status of apoptosis in PC-3 cells treated with aminophenol analogs, using annexin V, which binds to phosphatidylserine on the plasma membrane surface and propidium iodide (PI), which binds to DNA, by flow cytometric analysis. PC-3 cells treated with DMSO (control), 4 μM *p*-DDAP and 4 μM 4-HPR for 48 hr were stained with annexin V and PI, and were identified as being either viable (annexin V-negative and PI-negative, R1), early apoptotic (annexin V-positive and PI-negative, R2) or terminal apoptotic/necrotic (annexin V-positive and PI positive, R3). In control cells, only very small numbers of terminal apoptotic/necrotic cells (3.2%) were seen, and early apoptotic cells were only 2.7% of the total cell population (Fig. 3*a*). In contrast, the percentages of early apoptotic and terminal apoptotic/necrotic PC-3 cells treated with compounds were 9.5 and 29.4% for

p-DDAP and 3.5 and 7.4% for 4-HPR, respectively (Fig. 3*a*). These results indicate that *p*-DDAP and 4-HPR induce apoptosis of PC-3 cells, and that *p*-DDAP was a more potent inducer of apoptosis than 4-HPR.

Cell cycle changes in PC-3 cells treated with p-DDAP and 4-HPR

To evaluate whether growth inhibition and the induction of apoptosis in PC-3 cells by the treatment with *p*-DDAP (Figs. 2 and Fig. 3*a*) was caused by perturbations in the cell cycle progression, we determined the effects of *p*-DDAP on cell cycle distribution using a flow cytometer after PI staining of the cells. PC-3 cells were treated with DMSO (control), *p*-DDAP (1 μM, 10 μM) and 4-HPR (1 μM, 10 μM) for 48 hr. The control histogram in Figure 3*b* shows M1 corresponding to apoptotic sub-G_1, M2 to G_0/G_1, M3 to S-phase and M4 to G_2/M peaks with the sizes of subpopulations being given as percentages of total populations under the cell cycle histograms.

A sub-G_1 peak in the cell cycle profiles for PC-3 cells treated with *p*-DDAP and 4-HPR appeared in a dose-dependent manner. The emergence of a sub-G_1 peak indicated that cycle-arrested cells were undergoing apoptosis (Fig. 3*b*, M1). *p*-DDAP at concentrations of 1 and 10 μM markedly increased the population of sub-G_1 cells to 19.7 and 31.2% when compared with control 6.4%, while 1 and 10 μM 4-HPR gave no change or resulted in a slight increase to 5.5 and 8.5%, respectively. Increases of cell populations in sub-G_1 phase were significant in PC-3 cells treated with 1 and 10 μM *p*-DDAP and 10 μM 4-HPR. These results indicate that *p*-DDAP is an inducer of apoptosis in PC-3 cells with potency greater than 4-HPR.

A 48-hr incubation of PC-3 cells with 1 and 10 μM *p*-DDAP resulted in a statistically significant increase in the proportion of cells in S phase (Fig. 3*b*, M3) from 11.5% in control cultures to 20.1 and 30.4% in treated cultures, respectively. In contrast, in PC-3 cells treated with 10 μM 4-HPR for 48 hr, G_0/G_1 phase (Fig. 3*b*, M2) increased significantly from 65.0% in control cultures to 75.5% in treated cultures. These findings indicate that PC-3 cell apoptosis may be achieved by cell cycle arrest of S phase induced by *p*-DDAP and G_0/G_1 phase induced by 4-HPR. Thus, *p*-DDAP and 4-HPR arrest distinct phases in the cell cycle.

Activation of caspase 3 in PC-3 cells by treatment with p-DDAP and 4-HPR

Caspase 3 is a downstream enzyme in the apoptosis cascade. The activation of caspase 3 *via* the cleavage of intact caspase 3 (procaspase 3) by caspase 3 initiator is critical during apoptosis. Thus, we examined whether *p*-DDAP affects the activation of caspase 3 to the same extent as 4-HPR. PC-3 cells were grown in the presence of 10 μM *p*-DDAP and 4-HPR for 48 hr, and then cellular caspase 3 and procaspase 3 proteins were immunostained using anti-caspase 3 antibody. As shown in Figure 4*a*-a, the level of procaspase 3 exhibiting a molecular weight of 32 kDa in control cells was reduced ~64% in *p*-DDAP-treated cells and ~47% in 4-HPR-treated cells, while increases of the level of caspase 3, exhibiting molecular weight of 17 kDa, were not observed in either *p*-DDAP-treated or 4-HPR-treated cells. This indicates significant increases of caspase 3 cleavage level in PC-3 cells treated with both *p*-DDAP and 4-HPR. Next, we measured caspase 3 activity directly, since caspase 3 proteins could not detected by immunostaining. Figure 4*a*-b showed significant increases in caspase 3 activity in *p*-DDAP-treated cells (~2.5-fold) and 4-HPR-treated cells (~1.6-fold) when compared with control cells. These results suggest that both *p*-DDAP and 4-HPR activate the cleavage of procaspase 3 into caspase 3 with this rapid turn over leading to apoptosis in PC-3 cells.

Reduction of bcl-2 gene expression in PC-3 cells by treatment with p-DDAP and 4-HPR

The release of certain proteins from the mitochondria after caspase 3 activation affect the permeability of the mitochondria membrane. The bcl-2 family includes both pro- and antiapoptotic members. The latter includes bcl-2, bcl-X, bcl-w, A1 and Mcl-1 which associate with nuclear, mitochondria and endoplasmic membranes, and regulate permeability transition *via* transmembrane pores. As a follow up to our observation that *p*-DDAP induces caspase 3 activation, we examined whether *p*-DDAP affects *bcl-2* gene expression and the transition of proteins in the mitochondria. As shown in Figure 4*b*-a, *bcl-2* gene expression in PC-3 cells treated with *p*-DDAP and 4-HPR at a concentration of 10 μM, decreased in a time-dependent manner. Relative *bcl-2* mRNA expression (as a percentage of control) decreased to ~69 and 37% by the treatment with *p*-DDAP for 6 and 24 hr, respectively. In contrast, 4-HPR reduced *bcl-2* gene expression to ~70 and 60% for 6 and 24 hr, respectively (Fig. 4*b*-b). These results indicate that *p*-DDAP affects *bcl-2* expression in a time-dependent fashion to a greater extent than 4-HPR.

Antitumor effects against PC-3 tumors by the administration of p-DDAP

Antitumor efficacy *in vivo* of *p*-DDAP against PC-3 tumor was evaluated in comparison with 4-HPR by using distinct administration methods, i.p. and i.v. Athymic nude mice were first inoculated with PC-3 cells and given a vehicle, *p*-DDAP or 4-HPR by i.p. administration daily for 2 weeks. As shown in Figure 5*a*-a, rapid tumor growth was seen in control mice. In contrast, significant suppression of tumor growth was observed in mice administered with *p*-DDAP and 4-HPR. Next, we evaluated whether *p*-DDAP had antitumor efficacy against prostate cancer *in vivo* by other administration methods and schedules. PC-3 tumor-implanted mice were treated with microemulsions loading *p*-DDAP by i.v. daily for 5 days, when compared with mice treated with a single i.p. dose of *p*-DDAP. Figure 5*a*-b shows that antitumor effects on PC-3 tumor growth by i.v. administration of *p*-DDAP as well as by i.p. administration of *p*-DDAP were observed. Body weights of mice were not changed markedly during the administration of compounds (data not shown). Thus, *p*-DDAP was an extremely effective compound *in vivo* on tumor suppression against prostate cancer regardless of administration method and schedule.

Effects of p-DDAP on plasma retinol concentration

Finding of antitumor effects by *p*-DDAP led us to examine whether *p*-DDAP altered blood retinol levels. As shown in Figure 5*b*, the administration of 4-HPR induced a significant reduction (~81%) in plasma retinol concentration in rats, when compared with control rats. In contrast, there was little or no reduction of retinol levels in rats after the administration of *p*-DDAP. In addition, body weights of rats were not changed during the administration of compounds (data not shown). These results indicate that *p*-DDAP administration has little effect on plasma retinol levels *in vivo*.

Discussion

p-DDAP exhibits potent anticancer activity against hormonal resistant prostate cancer *in vitro* and *in vivo*, greater than 4-HPR, a well-known cancer chemopreventive and antiproliferative agent. In the current study, *p*-DDAP, whose design is based on structure–activity relationships of 4-HPR and lacks an aromatic ring needed for binding to RBP, showed excellent anticancer activity against human prostate cancer cell line PC-3 when compared with 4-HPR *in vitro* (Fig. 2). *p*-DDAP was the most potent antiproliferative agent against PC-3 cells among *p*-alkylaminophenols and 4-hydroxyphenyl analogs examined including 4-HPR and *p*-acylaminophenols. Growth of PC-3 cells was suppressed gradually in a

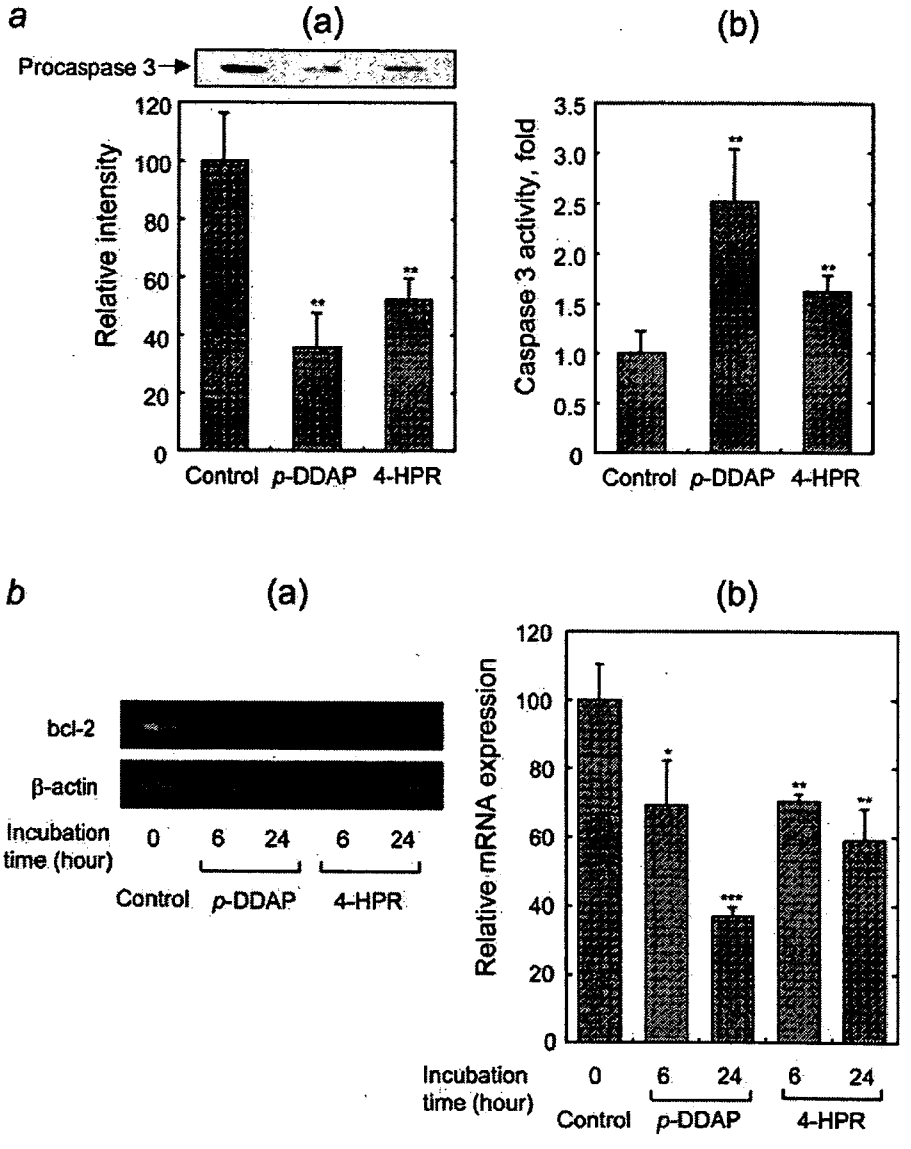

FIGURE 4 – Expression of Caspase 3 and *bcl-2* in PC-3 cells treated with *p*-DDAP and 4-HPR (*a*) PC-3 cells (5×10^4 cells/ml) were treated with DMSO (Control), 10 μM *p*-DDAP and 10 μM 4-HPR for 48 hr. After incubation, cells were harvested and lysed. Immunoblotting with anti-caspase 3 monoclonal antibody (a) and the measurement of caspase 3 activities (b) were performed as described under "Material and methods." The intensity or the activity of control was defined as 100% or 1, respectively. (*b*) PC-3 cells (5×10^4 cells/ml) were treated with DMSO (Control), 10 μM *p*-DDAP and 10 μM 4-HPR for 6 or 24 hr. Total RNA (5 μg) was prepared, and RT-PCR (30 cycles) was performed using specific primers against *bcl-2* as described under "Material and methods." After agarose gel (3%) electrophoresis (a), PCR products were analyzed by scanning densitometry (b). The *bcl-2* expression of control was defined as 100%. Results represent the mean of ± SD of each group. $*p < 0.05$, $**p < 0.01$, and $***p < 0.001$ *versus* control compared by Student's *t*-test.

dose-dependent manner from low to high concentration of *p*-DDAP. Cytotoxicity was observed by treatment with 4-HPR at high concentrations, but not by *p*-DDAP (Fig. 2). The data related to condensation nuclei, cytofluorimetric analysis, propidium iodide staining and the expression of *bcl-2* and caspase 3 (Figs. 2–4) showed that *p*-DDAP induced apoptosis of PC-3 cells *via* a bcl-2/caspase 3 cascade. *p*-DDAP arrested the S phase of the cell cycle, while 4-HPR arrested the G_0/G_1 phase. The administration of *p*-DDAP to mice implanted with PC-3 cells inhibited tumor growth *in vivo* with no change in body weight and plasma retinol levels (Fig. 5). These results suggest that *p*-DDAP exhibits superior anticancer potency against PC-3 prostate cancer *in vitro* and *in vivo*, and may have great clinical utility in the treatment of hormone-independent prostate cancer with reduced side effects.

Previous studies have shown that 4-HPR, a synthetic derivative of RA, is an effective chemopreventive and antiproliferative agent,[2–5] useful against a wide variety of tumor types. 4-HPR induces apoptosis in the human prostate cancer cell lines, LNCaP, DU-145 and PC-3,[32] as well as in human leukemia,[33,34] cervical carcinoma,[35,36] melanoma[37] and neuroblastoma[9,38] cell lines and primary meningioma.[39] These studies have shown that 4-HPR may induce cell apoptosis by a mechanism mediated through caspase-3 and bcl-2, which is distinct from the generation of reactive oxygen species. The design of *p*-DDAP is based on the structure of 4-HPR, and it exhibits the same side-chain length attached to the aminophenol residue as 4-HPR. In the current study, *p*-DDAP induced apoptosis (Figs. 2–4), activated caspase-3 and reduced *bcl-2* expression in PC-3 cells (Fig. 4). These results suggest that both *p*-DDAP and 4-HPR induce apoptosis of PC-3 cells by a mechanism mediated by the caspase cascade.

On the other hand, it is well known that 4-HPR affects the cell cycle, resulting in the inhibition of cell growth of a variety of cancer cell lines. In murine embryonal carcinoma (F9) cells, 4-HPR suppresses cell growth in the concentration range of 1–10 μM.[40] Flow cytometric analysis has revealed that 4-HPR increases the percentage of F9 cells in G_1 phase to the same extent as RA.[41–43] Thus, growth inhibition of F9 cells by 4-HPR results from G_1 cell cycle arrest. In addition, the effects of

a

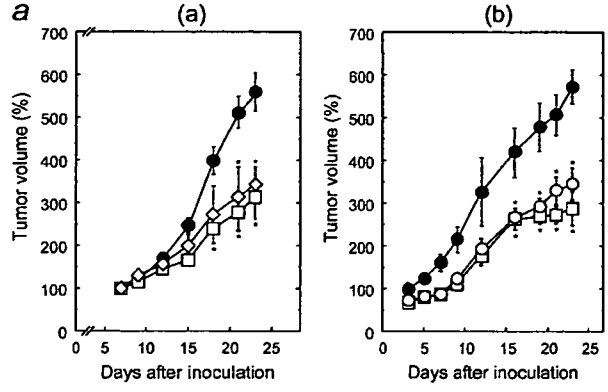

b

Treatment	Retinol (μg/ml)	% Change of retinol
Control	0.41 ± 0.02	-
p-DDAP	0.39 ± 0.02	- 5%
4-HPR	0.08 ± 0.02***	- 81%

FIGURE 5 – Effects of *p*-DDAP on PC-3 xenograft tumor growth and blood retinol concentration (*a*) Athymic nude mice were injected s.c. in the flank with PC-3 cells. Tumors had grown to an average volume of 50–100 mm^3. (a) Vehicle (Control, ●), 15 mg/kg *p*-DDAP (□) and 15 mg/kg 4-HPR (□) were injected to mice i.p. everyday for 2 weeks. (b) Microemulsions containing *p*-DDAP were injected to mice i.v. (○) 5 times at a dose of 10 mg/kg. *p*-DDAP was given to mice i.p. (□) at single dose of 40 mg/kg. The control (●) was given the same volume of vehicle. Tumor volumes were measured once every 2 or 3 days. (*b*) Sprague-Dawley rats were treated by i.p. injection with *p*-DDAP (12.5 mg/kg) and 4-HPR (12.5 mg/kg) every day for 7 days.[31] Plasma retinol levels were measured by HPLC as described under "Material and methods." Values for percent change of retinol were calculated with the following formula: —[(retinol concentration of control plasma) — (retinol concentration of experimental plasma)]/(retinol concentration of control plasma) × 100. Results represent the mean of ± SE of each group (n = 3–6). *$p < 0.05$ and ***$p < 0.001$ *versus* control compared by Student's *t*-test.

4-HPR on the growth and cell cycle of PC-3 cells have been evaluated previously.[44] PC-3 cells exposed to 4-HPR demonstrate a reduction in proliferation rate associated with the accumulation of cells in the G_0/G_1 phase of the cell cycle. Thus, inhibition of cancer cell growth by 4-HPR is a consequence of blocking the cell cycle transition from G_1 to S phase. These results are in agreement with the results of our current study (Fig. 3*b*). 4-HPR suppressed PC-3 cell growth, and induced apoptosis and the accumulation of cells in the cell cycle G_1 phase (Figs. 2–4). In contrast, *p*-DDAP exhibited potent antiproliferative activity of PC-3 cells in a dose-dependent manner and induced apoptosis (Figs. 2–4). However, the manner of cell cycle perturbation by *p*-DDAP was distinct from that by 4-HPR. The exposure of PC-3 cells to *p*-DDAP resulted in a statistically significant increase of cells in S phase, but not cells in G_1 phase. It would be interesting to identify key cell cycle proteins blocked by *p*-DDAP and examine whether the differences of growth inhibition and cytotoxicity between 4-HPR and *p*-DDAP can be attributed to the differences in the phase of cell cycle arrest.

Clinical studies have shown that treatment of patients with 4-HPR is accompanied by side effects that include night blindness due to decreasing serum retinol levels.[12] This side effect seems to be due to insufficient supply of retinol to the eyes resulting from the displacement of retinol from serum RBP.[13–15,45] 4-HPR exhibits extremely poor binding to nuclear retinoid receptors but not to RBP, and it shows anticancer activity against cells resistant to RA. 4-HPR may act on cells directly rather than through hydrolysis to free RA. Several nonhydrolyzable compounds were synthesized and evaluated for side effects, compared with 4-HPR. 4-Hydroxybenzylretinone (4-HBR), a stable C-linked analog of 4-HPR that cannot be hydrolyzed to RA was synthesized. It was shown to exhibit antitumor effects similar to 4-HPR but without side effects of night blindness, despite the fact that 4-HBR binds to RBP to the same extent as 4-HPR.[46,47] In addition, 4-HPR-C-glucuronide (4-HPRCG), a C-linked analog of 4-HPR-glucuronide that cannot be hydrolyzed to 4-HPR, is an effective chemopreventive agent with almost no side effects. However, 4-HPRCG shows less antitumor activity and cytotoxity than 4-HPR.[31,48] Both 4-HBR and 4-HPRCG contain the same aromatic ring as retinol, RA and 4-HPR, and they may still affect endogenous retinol levels in the body, since RBP recognizes and binds the aromatic ring of retinol. In the current study, *p*-DDAP, which lacks an aromatic ring, exhibits a markedly distinct structure compared to retinol, RA, 4-HPR, 4-HBR and 4-HPRCG, yet it shows potent antiproliferative and antitumor activities against prostate cancer *in vitro* and *in vivo* greater than 4-HPR (Figs. 2–4). *p*-DDAP inhibits PC-3 cell growth gradually from low to high concentrations when compared to 4-HPR, indicating that *p*-DDAP is more potent than 4-HPR. It would be interesting to further examine the anticancer activities of *p*-DDAP against other tumor models, such as animal models of metastatic cancer using the murine reticulosarcoma cell line (M5076)-implanted mouse as well as carcinogenesis using 17,12-dimethylbenz(a)anthracene (DMBA)-induced mammary tumors. Studies are presently underway to measure the effectiveness of *p*-DDAP against other animal tumor models.

Previous reports have shown that *p*-alkylaminophenols containing *p*-DDAP exhibit antioxidant activities.[17,19,21] *p*-Alkylaminophenols including *p*-DDAP (Fig. 1) and *p*-DAP, but not 4-HPDD (Fig. 1) and 4-HPD, exhibit superoxide scavenging activities.[19] Elongation of the alkyl chain length (*p*-DDAP and *p*-DAP) reduce superoxide trapping capability. In contrast, lipid peroxidation in rat liver microsomes is reduced by *p*-DDAP and *p*-DAP in dose-dependent manners. 4-HPDD and 4-HPD are extremely poor inhibitors of lipid peroxidation, being ~400–1,300-fold lower than *p*-DDAP and *p*-DAP. These results suggest that the novel compound *p*-DDAP is an extremely effective antioxidant. Anticancer activities of *p*-DDAP in the current study (Figs. 2–5) are appeared to be correlated with inhibitory potency against lipid peroxidation, but not with superoxide scavenging activity. The presence of carbonyl moieties in the *p*-alkylaminophenols diminished their capabilities as anticancer agents (Fig. 2*b*) and antioxidants as measured by lipid peroxidation inhibition. On the other hand, mitochondrial lipid peroxidation was inhibited by retinoids (retinol, retinol acetate, 4-HPR, retinol palmitate and retinal) only at high concentrations (0.1–10 mM).[49] In contrast, 13-*cis*-retinoic acid, 4-HPR and *p*-DDAP suppress microsomal lipid peroxidation with IC_{50} values of 10,[50] 3.2 (Refs. 17 and 21) and 0.0155 μM,[19] respectively. It was found that *p*-DDAP is a more potent inhibitor of lipid peroxidation, having ~200-fold higher potency than 4-HPR. Anticancer activities of *p*-DDAP and 4-HPR in the current study seemed to be related to inhibitory potency against lipid peroxidation. Consequently, antitumor effects of *p*-DDAP may be in part mediated by antioxidant activities.

p-DDAP is an extremely effective anticancer drug *in vitro* and *in vivo* against prostate cancer. The alkyl residue of *p*-DDAP may be particularly significant for association with cell membranes and localization to active sites in cells, where anticancer action, or antioxidant action, the inhibition of lipid peroxidation can occur. The results reported herein may suggest potential clinical application of *p*-DDAP in cancer patients.

Acknowledgements

We thank Dr. Terrence Burke, Jr, for helpful comments.

References

1. Takahashi N, Sausville EA, Breitman TR. *N*-(4-Hydroxyphenyl) retinamide (fenretinide) enhances retinoic acid-induced differentiation and retinoylation of proteins. Clin Cancer Res 1995;1:637–42.
2. Abou-Issa H, Webb TE, Minton JP, Moeschberger M. Chemotherapeutic evaluation of glucarate and *N*-(4-hydroxyphenyl)retinamide alone and in combination in the rat mammary tumor model. J Natl Cancer Inst 1989;81:1820–3.
3. Meyskens F, Jr, Alberts DS, Salmon SE. Effect of 13-*cis*-retinoic acid and 4-hydroxyphenyl-all-*trans*-retinamide on human tumor colony formation in soft agar. Int J Cancer 1983;32:295–9.
4. Moon RC, Metha RG, Rao KVN. The Retinoids: biology, chemistry, and medicine. In: Sporn MB, Roberts AB, Goodman DS, eds. Retinoids and cancer in experimental animals. New York: Raven Press, 1994.573–95.
5. Pienta KJ, Nguyen NM, Lehr JE. Treatment of prostate cancer in the rat with the synthetic retinoid fenretinide. Cancer Res 1993;53:224–6.
6. Decensi A, Fontana V, Fioretto M, Rondanina G, Torrisi R, Orengo MA, Costa A. Long-term effects of fenretinide on retinal function. Eur J Cancer 1997;33:80–4.
7. Decensi A, Bruno S, Costantini M, Torrisi R, Curotto A, Gatteschi B, Nicolo G, Polizzi A, Perloff M, Malone WF, Bruzzi P. Phase IIa study of fenretinide in superficial bladder cancer, using DNA flow cytometry as an intermediate end point. J Natl Cancer Inst 1994;86:138–40.
8. Rotmensz N, De Palo G, Formelli F, Costa A, Marubini E, Campa T, Crippa A, Danesini GM, Delle Grottaglie M, Di Mauro MG, Filiberti A, Gallazzi M, et al. Long-term tolerability of fenretinide (4-HPR) in breast cancer patients. Eur J Cancer 1991;27:1127–31.
9. Reynolds CP. Differentiating agents in pediatric malignancies: retinoids in neuroblastoma. Curr Oncol Rep 2000;2:511–8.
10. Veronesi U, De Palo G, Costa A, Formelli F, Decensi A. Chemoprevention of breast cancer with fenretinide. IARC Sci Publ 1996; 136:87–94.
11. Vaishampayan U, Heilbrun LK, Parchment RE, Jain V, Zwiebel J, Boinpally RR, LoRusso P, Hussain M. Phase II trial of fenretinide in advanced renal carcinoma. Invest New Drugs 2005;23:179–85.
12. Formelli F, Carsana R, Costa A, Buranelli F, Campa T, Dossena G, Magni A, Pizzichetta M. Plasma retinol level reduction by the synthetic retinoid fenretinide: a 1 year follow-up study of breast cancer patients. Cancer Res 1989;49:6149–52.
13. Costa A, Malone W, Perloff M, Buranelli F, Campa T, Dossena G, Magni A, Pizzichetta M, Andreoli C, Del Vecchio M, Formelli F, Barbieri A. Tolerability of the synthetic retinoid Fenretinide (HPR). Eur J Cancer Clin Oncol 1989;25:805–8.
14. Formelli F, Clerici M, Campa T, Di Mauro MG, Magni A, Mascotti G, Moglia D, De Palo G, Costa A, Veronesi U. Five-year administration of fenretinide: pharmacokinetics and effects on plasma retinol concentrations. J Clin Oncol 1993;11:2036–42.
15. Kaiser-Kupfer MI, Peck GL, Caruso RC, Jaffe MJ, DiGiovanna JJ, Gross EG. Abnormal retinal function associated with fenretinide, a synthetic retinoid. Arch Ophthalmol 1986;104:69–70.
16. Takahashi N. Antioxidant properties of *N*-(4-hydroxyphenyl)retinamide (fenretinide). Biol Pharm Bull 2000;23:222–5.
17. Takahashi N, Ohba T, Togashi S, Fukui T. Biological activities of *p*-methylaminophenol, an essential structural component of *N*-(4-hydroxyphenyl)retinamide, fenretinide. J Biochem (Tokyo) 2002;132: 767–74.
18. Takahashi N, Honda T, Ohba T. Anticancer and superoxide scavenging activities of *p*-alkylaminophenols having various length alkyl chains. Bioorg Med Chem 2006;14:409–17.
19. Takahashi N, Ohba T, Yamauchi T, Higashiyama K. Antioxidant and anticancer activities of novel *p*-alkylaminophenols and *p*-acylaminophenols (aminophenol analogs). Bioorg Med Chem 2006;14:6089–96.
20. Ohba T, Yamauch T, Higashiyama K, Takahashi N. Potent anticancer activities of novel aminophenol analogs against various cancer cell lines. Bioorg Med Chem 2007;15:847–53.
21. Takahashi N, Tamagawa K, Kubo Y, Fukui T, Wakabayashi H, Honda T. Enhancement of antioxidant activity of *p*-alkylaminophenols by alkyl chain elongation. Bioorg Med Chem 2003;11:3255–60.
22. Collins SJ, Gallo RC, Gallagher RE. Continuous growth and differentiation of human myeloid leukemic cells in suspension culture. Nature 1977;270:347–9.
23. Robertson KA, Emami B, Mueller L, Collins SJ. Multiple members of the retinoic acid receptor family are capable of mediating the granulocytic differentiation of HL-60 cells. Mol Cell Biol 1992;12:3743–9.
24. Batist G, Tulpule A, Sinha BK, Katki AG, Myers CE, Cowan KH. Overexpression of a novel anionic glutathione transferase in multidrug-resistant human breast cancer cells. J Biol Chem 1986;261: 15544–9.
25. Cohen LH, Griffioen M, Havekes L, Schouten D, van Hinsbergh V, Kempen HJ. Effects of compactin, mevalonate and low-density lipoprotein on 3-hydroxy-3-methylglutaryl-coenzyme A reductase activity and low-density-lipoprotein-receptor activity in the human hepatoma cell line Hep G2. Biochem J 1984;222:35–9.
26. Stone KR, Mickey DD, Wunderli H, Mickey GH, Paulson DF. Isolation of a human prostate carcinoma cell line (DU 145). Int J Cancer 1978;21:274–81.
27. Alley MC, Scudiero DA, Monks A, Hursey ML, Czerwinski MJ, Fine DL, Abbott BJ, Mayo JG, Shoemaker RH, Boyd MR. Feasibility of drug screening with panels of human tumor cell lines using a microculture tetrazolium assay. Cancer Res 1988;48:589–601.
28. Wang J, Maitani Y, Takayama K. Antitumor effects and pharmacokinetics of aclacinomycin A carried by injectable emulsions composed of vitamin E, cholesterol, and PEG-lipid. J Pharm Sci 2002;91:1128–34.
29. Shiokawa T, Hattori Y, Kawano K, Ohguchi Y, Kawakami H, Toma K, Maitani Y. Effect of polyethylene glycol linker chain length of folate-linked microemulsions loading aclacinomycin A on targeting ability and antitumor effect in vitro and in vivo. Clin Cancer Res 2005;11:2018–25.
30. Formelli F, Cleris L. Synthetic retinoid fenretinide is effective against a human ovarian carcinoma xenograft and potentiates cisplatin activity. Cancer Res 1993;53:5374–6.
31. Alshafie GA, Walker JR, Curley R, Jr, Clagett-Dame M, Highland MA, Nieves NJ, Stonerock LA, Abou-Issa H. Inhibition of mammary tumor growth by a novel nontoxic retinoid: chemotherapeutic evaluation of a C-linked analog of 4-HPR-glucuronide. Anticancer Res 2005;25:2391–8.
32. Shimada K, Nakamura M, Ishida E, Kishi M, Yonehara S, Konishi N. Contributions of mitogen-activated protein kinase and nuclear factor κ B to *N*-(4-hydroxyphenyl)retinamide-induced apoptosis in prostate cancer cells. Mol Carcinog 2002;35:127–37.
33. Delia D, Aiello A, Formelli F, Fontanella E, Costa A, Miyashita T, Reed JC, Pierotti MA. Regulation of apoptosis induced by the retinoid *N*-(4-hydroxyphenyl) retinamide and effect of deregulated bcl-2. Blood 1995;85:359–67.
34. DiPietrantonio AM, Hsieh TC, Juan G, Traganos F, Darzynkiewicz Z, Wu JM. Fenretinide-induced caspase 3 activity involves increased protein stability in a mechanism distinct from reactive oxygen species elevation. Cancer Res 2000;60:4331–5.
35. Suzuki S, Higuchi M, Proske RJ, Oridate N, Hong WK, Lotan R. Implication of mitochondria-derived reactive oxygen species, cytochrome C and caspase-3 in *N*-(4-hydroxyphenyl)retinamide-induced apoptosis in cervical carcinoma cells. Oncogene 1999;18:6380–7.
36. Oridate N, Suzuki S, Higuchi M, Mitchell MF, Hong WK, Lotan R. Involvement of reactive oxygen species in *N*-(4-hydroxyphenyl)retinamide-induced apoptosis in cervical carcinoma cells. J Natl Cancer Inst 1997;89:1191–8.
37. Montaldo PG, Pagnan G, Pastorino F, Chiesa V, Raffaghello L, Kirchmeier M, Allen TM, Ponzoni M. *N*-(4-hydroxyphenyl) retinamide is cytotoxic to melanoma cells in vitro through induction of programmed cell death. Int J Cancer 1999;81:262–7.
38. Lovat PE, Oliverio S, Corazzari M, Rodolfo C, Ranalli M, Goranov B, Melino G, Redfern CP, Piacentini M. Bak: a downstream mediator of fenretinide-induced apoptosis of SH-SY5Y neuroblastoma cells. Cancer Res 2003;63:7310–3.
39. Puduvalli VK, Li JT, Chen L, McCutcheon IE. Induction of apoptosis in primary meningioma cultures by fenretinide. Cancer Res 2005; 65:1547–53.
40. Sabichi AL, Xu H, Fischer S, Zou C, Yang X, Steele VE, Kelloff GJ, Lotan R, Clifford JL. Retinoid receptor-dependent and independent biological activities of novel fenretinide analogs and metabolites. Clin Cancer Res 2003;9:4606–13.
41. Chiba H, Clifford J, Metzger D, Chambon P. Specific and redundant functions of retinoid X receptor/retinoic acid receptor heterodimers in differentiation, proliferation, and apoptosis of F9 embryonal carcinoma cells. J Cell Biol 1997;139:735–47.
42. Chiba H, Clifford J, Metzger D, Chambon P. Distinct retinoid X receptor-retinoic acid receptor heterodimers are differentially involved in the control of expression of retinoid target genes in F9 embryonal carcinoma cells. Mol Cell Biol 1997;17:3013–20.
43. Clifford J, Chiba H, Sobieszczuk D, Metzger D, Chambon P. RXRalpha-null F9 embryonal carcinoma cells are resistant to the differentiation, anti-proliferative and apoptotic effects of retinoids. EMBO J 1996;15:4142–55.
44. Igawa M, Tanabe T, Chodak GW, Rukstalis DB. *N*-(4-Hydroxyphenyl) retinamide induces cell cycle specific growth inhibition in PC3 cells. Prostate 1994;24:299–305.
45. Berni R, Stoppini M, Zapponi MC. The piscine plasma retinol-binding protein. Purification, partial amino acid sequence and interac-

tion with mammalian transthyretin of rainbow trout (*Oncorhynchus mykiss*) retinol-binding protein. Eur J Biochem 1992;204:99–106.
46. Weiss KL, Alshafie G, Chapman JS, Mershon SM, Abou-Issa H, Clagett-Dame M, Curley R, Jr. An unhydrolyzable analog of *N*-(4-hydroxyphenyl)retinamide. synthesis and preliminary biological studies. Bioorg Med Chem Lett 2001;11:1583–6.
47. Abou-Issa H, Curley RW, Jr, Alshafie GA, Weiss KL, Clagett-Dame M, Chapman JS, Mershon SM. Chemotherapeutic evaluation of 4-hydroxybenzylretinone (4-HBR), a nonhydrolyzable C-linked analog of *N*-(4-hydroxyphenyl) retinamide (4-HPR) against mammary carcinogenesis. Anticancer Res 2001;21:3839–44.
48. Walker JR, Alshafie G, Nieves N, Ahrens J, Clagett-Dame M, Abou-Issa H, Curley R, Jr. Synthesis and preliminary chemotherapeutic evaluation of the fully C-linked glucuronide of *N*-(4-hydroxyphenyl)-retinamide. Bioorg Med Chem 2006;14:3038–48.
49. Das NP. Effects of vitamin A and its analogs on nonenzymatic lipid peroxidation in rat brain mitochondria. J Neurochem 1989;52:585–8.
50. Samokyszyn VM, Marnett LJ. Inhibition of microsomal lipid peroxidation by 13-*cis*-retinoic acid. Methods Enzymol 1990;190:281–8.

Magnetic targeting after femoral artery administration and biocompatibility assessment of superparamagnetic iron oxide nanoparticles

Hui-Li Ma,[1] Xian-Rong Qi,[1] Wu-Xiao Ding,[1] Yoshie Maitani,[2] Tsuneji Nagai[2]
[1]*Department of Pharmaceutics, School of Pharmaceutical Sciences, Peking University, Beijing 100083, China*
[2]*Institute of Medicinal Chemistry, Hoshi University, Shinagawa-Ku, Tokyo 142-850, Japan*

Received 14 October 2006; revised 22 December 2006; accepted 30 January 2007
Published online 6 July 2007 in Wiley InterScience (www.interscience.wiley.com). DOI: 10.1002/jbm.a.31346

Abstract: Ferrofluids are attractive candidates for magnetic targeting system because of their fluidity and magnetism. The magnetic nanoparticles in ferrofluids should have combined properties of superparamagnetic behavior, target localization, and biocompatibility. The magnetic targeting and biocompatibility of superparamagnetic iron oxide nanoparticles stabilized by alginate (SPION-alginate) was investigated *in vitro* and *in vivo*. The localization of SPION-alginate by an external magnetic field *in vitro* was quantitatively evaluated by determining the iron content, and the results revealed that the localization ratio of SPION-alginate was 56%. Magnetic targeting of the SPION-alginate after femoral artery administration with the magnetic field in rats was quantitatively investigated by iron content and qualitatively confirmed by histological evaluation and magnetic resonance imaging. The ratio of iron content between the target site and the nontarget site were 8.88 at 0.5 h and 7.50 at 2 h, respectively. The viability of RAW264.7 cells and L929 cells was apparently unaltered upon exposure to SPION-alginate. The incubation with erythrocytes indicated that the SPION-alginate did not induce erythrocytes hemolysis and aggregation. In conclusions, the SPION-alginate had magnetic targeting with an external magnetic field and did not be detained at the injection site without the magnetic field. The SPION-alginate was generally considered to be biocompatible in cytotoxicity and hemolysis aspects. © 2007 Wiley Periodicals, Inc. J Biomed Mater Res 84A: 598–606, 2008

Key words: superparamagnetic iron oxide nanoparticles (SPION); magnetic targeting; biocompatibility; alginate; localization ratio

INTRODUCTION

Drug targeting always attracts the most interests from pharmaceutical researchers, among which magnetic drug targeting has been widely studied for the advantages to reduce the amount of drug needed and to reduce the adverse effect of drug. In magnetic targeting, a magnetic compound was injected into the systemic circulation, and then stopped with a powerful magnetic field in the target site.[1] Compared with other targeting vectors, such as ligand-targeting particulates and enzyme-triggered drug release system, magnetic targeting system is feasible to produce, reliable to control and can be specifically modified for drug delivery applications. Current applications of magnetic targeting system include magnetic delivery of chemotherapy drugs to tumors,[2–4] magnetic targeting of radioisotope,[1,5] magnetic hyperthermia,[6] magnetically enhanced gene therapy,[7] and magnetic embolization.[8] Some successes are achieved, but the results from both laboratory and clinical trials are far from satisfactory. Currently, one of the main problems is that the localization effect of magnetic carrier in target site with the magnetic field is not as good as expected.

Many factors, including physio-chemical properties of magnetic carrier, target sites, magnetic field, and the route of administration, can affect the magnetic targeting effect. When addressing the physiochemical properties of magnetic carrier, we have to consider the size, magnetization and matrix materials. Magnetic carriers can be grouped into ferrofluids, magnetic nanospheres, and magnetic microspheres according to the size from 10 nm to 100 μm. Ferrofluids are stable colloidal systems that com-

Correspondence to: X.R. Qi; e-mail: qixr2001@yahoo.com.cn
Contract grant sponsor: National High Technology Research and Development Program of China; contract grant number: 863 Program, No. 2003AA326020

posed of solid, magnetic, single-domain magnetic nanoparticles, typically between 3 and 15 nm in diameter, in a nonmagnetic solvent.[9] Because of the fluidity and magnetism of ferrofluids, they have been widely used in the magnetic targeting system. For biomedical applications, it is required that the magnetic nanoparticles should have combined properties of superparamagnetic behavior, high magnetic saturation, good stability, target localization ability, and biocompatibility. In our laboratory, a kind of ferrofluids, superparamagnetic iron oxide nanoparticles stabilized by alginate (SPION-alginate), was prepared successfully. They were composed of iron oxide (Fe_3O_4) with 5–10 nm core diameter and had good magnetic susceptibility.[10]

The magnetic field should be of sufficient strength to attract the magnetic particles into the desired area or target site. The higher magnetic flux density and magnetic gradient it is, the better the location effect is.[2] Because of the superparamagnetism and liquid state of ferrofluids, the magnetism of ferrofluids was usually weaker than that of magnetic microsphere. Therefore, a higher magnetic field is needed to attract or hold the injected ferrofluids to the target site.

The route of administration and target site can also greatly affect the magnetic targeting effect. If the target site is a part of reticuloendothelial system (RES), such as liver or spleen, most of magnetic carriers always accumulate in it by the passive targeting effect through intravenous injection. If the target site is a tumor outside RES, the passive accumulation in RES becomes a significant negative factor, and this is one reason why magnetic targeting carrier is still far from satisfactory. Compared with intravenous injection, the artery injection has more advantages, since the magnetic carriers have more chances to access to the target site, avoid clearance by RES, and then stopped by external magnetic filed.[2–4]

The term "biocompatibility" encompasses many different properties of the materials, however, two important aspects of the biomaterial screening refer to their *in vitro* cytotoxicity and blood compatibility behavior.[11] The cell lines of mouse fibroblasts (L929) and mouse macrophages (RAW264.7) were widely used in biocompatibility studies. L929 was recommended by many standard institutions as reference cell line for the cytotoxicity testing of polymers[12,13] and RAW264.7 was used for uptake iron oxide nanoparticles.[14]

In this study, we evaluated the magnetic targeting of SPION-alginate with the magnetic field both *in vitro* and *in vivo*. Biocompatibility of SPION-alginate was measured by hemolysis assay and erythrocytes aggregation assay, and *in vitro* cytotoxicity of L929 cells and RAW264.7 cells. Meanwhile, the labeling of RAW264.7 cells with SPION-alginate was examined.

MATERIALS AND METHODS

Chemicals and magnetic field

The SPION-alginate was a kind of superparamagnetic iron oxide nanoparticles stabilized by alginate macromolecules with good stability and good magnetism.[10] The SPION-alginate was prepared by a modified two-step coprecipitation method. The ferric and ferrous chlorides (molar ratio of 2:1.5) were dissolved in distilled water and chemical precipitation was achieved by adding 5 mol/L NaOH solution at 60°C. The sodium alginate solution was added to the suspension and was stirred vigorously for 30 min. The mixture was heated at 80°C with slow stirring for 1 h and then sonicated for 20 min. All the above processes were run under total N_2 protection. The obtained suspension was dialyzed against deionized water. Finally, the suspension was centrifuged at 10,000 rpm for 20 min to remove the solid material, and the black supernatant, namely SPION-alginate, was collected.

The SPION-alginate had a core (iron oxide nanoparticles) diameter of 5–10 nm, a hydrodynamic diameter of 193.8 nm, and ξ-potential of −67.5 mV. Saturation magnetization (Ms) of the SPION-alginate in suspension was 40 emu/g at 27°C. T1 relaxivity and T2 relaxivity in 0.9% NaCl solution determined by a 1.5 T MRI scanner at 20°C were 7.86 ± 0.20 s^{-1} mM^{-1} and 281.2 ± 26.4 s^{-1} mM^{-1}, respectively.[10]

A cuboid permanent neodymium iron boron magnet (NdFeB-permanent magnet) with length, width, and height of 33, 22, and 11 mm, respectively, was purchased from Beijing Sheng Magnetic Science & Tech (Beijing, China). The magnet with the surface magnetic field of 3500 G was used to produce the magnetic field. And all other reagents used were of analytical reagent grade.

Localization of SPION-alginate with magnetic field *in vitro*

The apparatus of localization of SPION-alginate with external magnetic field *in vitro* was shown in Figure 1. At first, the roller pump was turned on and the rate of distilled water (flow medium) was set to 8 mL/min and 0.5 mL SPION-alginate of 6.04 mg Fe/mL was injected at

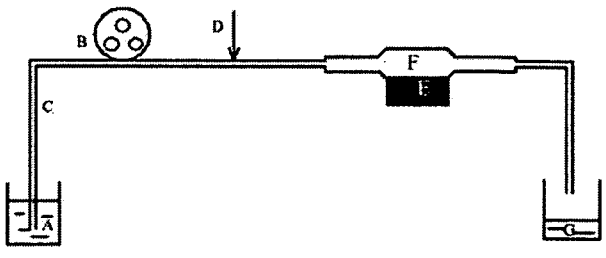

Figure 1. The *in vitro* apparatus of location of SPION-alginate with the external magnetic field. (A) flow medium (distilled water, 8 mL/min); (B) roller pump; (C) rubber tube; (D) injection site of SPION-alginate; (E) magnet; (F) glass tube; (G) eluted medium.

the injection part in the rubber tube. At 10 min after circulation, the glass tube with magnet was erected gently to pour the iron oxide particles unlocated tightly. The remnants of SPION-alginate in the glass tube captured by the magnet were separated, and 6*M* HCl solution was added to dissolve the iron oxide nanoparticles. The iron content was measured by *o*-phenanthroline method.[15] The ratio of iron content captured by the magnet to injected one was referred to as localization ratio *in vitro*. The experiment was repeated in triplicate.

Magnetic targeting evaluation *in vivo*

Male Sprague–Dawley rats weighing 250 ± 20 g were purchased from Department of Laboratory Animal Science of Peking University Health Science Center. NIH guidelines for the care and use of laboratory animals (NIH Publication #85-23 Rev. 1985) have been observed. Rats were divided into two groups randomly. One group was operated with magnetic field at the right thigh. Before the magnetic targeting of SPION-alginate was carried out, rats were anesthetized by intraperitoneal injection of 1.5 g/kg of ethyl carbamate. The right thigh was disinfected with iodine tincture and 70% alcohol by turns, 30,000 IU penicillin was given by intramuscular injection, and the femoral artery was separated. The SPION-alginate at a dose of 12 mg Fe/kg body weight was injected into the femoral artery at the right thigh under the magnetic field. When the magnetic targeting was performed, the distance between the magnet and the target site was 3 mm, the magnetic field intensity at the target site was 3000 G determined by Gaussmeter, and the magnetic field gradient was 2000 G/cm. The magnetization of SPION-alginate in suspension under the applied magnetic field of 3000 G was 36 emu/g.

After the magnetic targeting, rats were sacrificed by being cut abdominal aorta. The right thigh with magnetic field was referred to as the target site and the left thigh without magnetic field was referred to as the nontarget site in this paper. The right thigh (the target site), left thigh (the nontarget site), liver, and spleen of rats were immediately collected and frozen at −20°C until analysis. Concerning the thigh of rat, the leg was cut from inguinal groove to knee joint to get thigh part, and the thigh was decorticated, followed by removing the bone, separating the muscle of the thigh. Another group was operated without magnetic field at the right thigh, and other conditions were the same as the group with magnetic filed. The iron content in the right thigh, the left thigh, liver, and spleen were determined as follows. The tissues were digested in a beaker with the mixture acid of HNO_3-$HClO_4$ (4:1 v:v) for 48 h at room temperature, and then the solution was evaporated to dryness in sand bath at 100°C. Finally 37.5% HCl was added to the beaker to dissolve the solid and the iron content was determined by *o*-phenanthroline method. The ratio of iron content retained at the right thigh to that of injected was regarded as the localization ratio *in vivo*.

After the magnetic targeting, some of the right thigh (the target site) was intersected, embedded in 4% paraformaldehyde solution (pH 7.4), and then observed at light microscopy after Perls staining and hematoxylin and eosin (H&E) staining.

Ten hours after SPION-alginate application with or without magnetic field on the right thigh, magnetic resonance imaging (MRI) was performed on a 3.0 T clinical MR scanner (GE HD, Milwaukee, WI) with a GPFLEX coil. T2*-weighted gradient recalled echo (GRE) sequence with a coronary plane was used for imaging with the following parameters: repetition time (TR) of 460 ms; echo time (TE) of 6.6 ms; flip angle of 25°; bandwith of 62.5 kHz; field of view of 10 × 10 cm, slice thickness of 3 mm with no gap; matrix of 256 × 128.

Hemolysis assay *in vitro*

A hemolysis test was performed following the procedure reported previously.[16] The rabbit erythrocyte suspension in 0.9% NaCl (2% (v/v)) was prepared. The SPION-alginate of different concentrations, 0.9% NaCl solution (negative control group as 0% hemolysis) or distilled water (positive control group as 100% hemolysis) was added to the erythrocyte suspension and they were incubated for 3 h at 37°C. After centrifugation at 4000 rpm for 10 min, the absorbance of the supernatant was determined at 540 nm to evaluate the leakage of hemoglobin. Percentage of hemolysis was calculated by $(A_S - A_N - A_{SB})/(A_P - A_N) \times 100\%$, where A_S was the average absorbance of the SPION-alginate in erythrocyte suspension, A_N was the average absorbance of 0.9% NaCl solution in erythrocyte suspension (0% hemolysis), A_P was the average absorbance of distilled water in erythrocyte suspension (100% hemolysis). Because the SPION-alginate still had some extent absorbance at 540 nm after centrifugation, so the average absorbance of SPION-alginate only in 0.9% NaCl solution (A_{SB}) is introduced to the equation in order to eliminate the effect of SPION-alginate itself. The experiment was done in triplicate.

Erythrocytes aggregation assay

Rabbit erythrocytes suspension 200 μL was mixed with the indicated amount of SPION-alginate and incubated for 1 h at 37°C in a 24-well plate. The plate was examined by an inverted microscope (Leica DMIRE2, Germany).

Cell culture

L929 cells and RAW264.7 cells were cultured in RPMI 1640 medium (Gibco-Invitrogen, NY) supplemented with 10% (v/v) heat-inactivated newborn calf serum (NCS) (Hyclone, USA), 200 U/mL penicillin, 100 U/mL streptomycin, and 0.11 mg/mL sodium pyruvate. Cells were all maintained in a 5% CO_2 atmosphere at 37°C.

In vitro cytotoxicity evaluation

To determine cytotoxicity, a 3-(4,5-dimethylthiazol-2-yl)-2,5-diphenyl tetrazolium bromide (MTT) assay was performed.[17] The cells were plated at a density of 5×10^4 cells/well for RAW264.7 and 3×10^4 cells/well for L929 in 96-well plate and cultured for 24 h at 37°C in a 5% CO_2 atmosphere. For cytotoxicity without NCS, the medium in

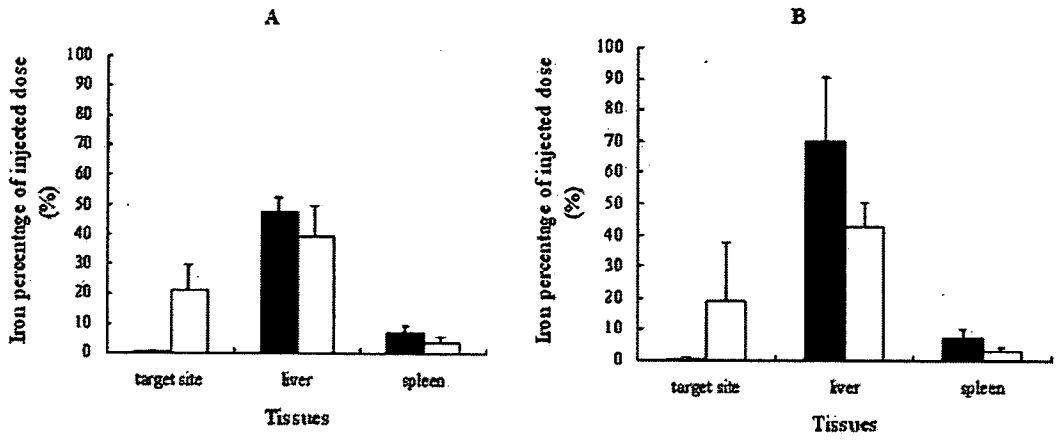

Figure 2. The iron percentage of injected SPION-alginate in target site, liver, and spleen with (□) or without (■) 3500 G magnetic field at 0.5 h (A) or 2 h (B) after femoral arterial injection of SPION-alginate at a dose of 12 mg Fe/kg. Data represent mean ± SD ($n = 3$).

the wells was replaced with 90 μL RPMI 1640 medium, 24 h later, 10 μL serial dilutions of the SPION-alginate were added to cells for 24 h with final iron concentrations from 6.25 to 100.0 μg/mL, and 10 μL RPMI 1640 medium was added to cells as control sample. For cytotoxicity with NCS, the medium in the wells was replaced with 90 μL RPMI 1640 medium with 10% NCS and 10 μL serial dilutions of SPION-alginate were added with the same iron concentrations as mentioned earlier for 24 h. The cells were washed once with phosphate-buffered saline (PBS, pH 7.4) and replenished with 100 μL medium, and then 10 μL MTT solution (Sigma, USA) at 5 mg/mL in saline solution was added to each well. After 4 h of incubation, the medium was removed and formazan crystals were solubilized with dimethylsulphoxide (DMSO) for 10 min at room temperature. The absorbance of each well was then measured on a microplate reader (Bio-Rad Model 550, USA) at a wavelength of 570 nm, with 655 nm as a reference wavelength. The relative cell viability (%) related to control wells was calculated by $(A_{test}/A_{control}) \times 100\%$. where A_{test} was the absorbance of the test sample and $A_{control}$ was the absorbance of control sample. The experiments were run in hexakis and were repeated three times.

Cell labeling with SPION-alginate

RAW264.7 cells were seeded at a density of 5×10^4 cells/mL in 35-mm culture plate at 37°C in a 5% CO_2 atmosphere. After 24 h, the SPION-alginate was added to cells with final iron cation concentrations ranging from 12.5 to 50.0 μg/mL for various incubation times (1–24 h). And then the cells were washed with PBS to remove excess SPION-alginate. For Prussian blue staining, which indicated the presence of iron, the cells were fixed with 4% glutaraldehyde (Merck, Germany) for 10 min and were washed with PBS, followed by incubation with 2% potassium ferrocyanide in 6% HCl for 30 min. After the wash, they were counterstained with nuclear fast red for 5 min.[18] The specimens were then examined under a light microscope (Olympus BH2, Japan).

RESULTS

Localization of SPION-alginate with magnetic field *in vitro*

From the iron content of SPION-alginate captured by the magnet, the localization ratio *in vitro* was (56 ± 5.1)% ($n = 3$).

Magnetic targeting evaluations *in vivo*

Figure 2 showed the iron accumulation in target site, liver and spleen with or without magnetic field via femoral artery injection of SPION-alginate at a dose of 12 mg Fe/kg. At 0.5 h [Fig. 2(A)] and 2 h [Fig. 2(B)] after injection, the localization ratios *in vivo* were about 20%, the iron contents in the right thigh (the target site) with magnetic field were significantly higher than those in the left thigh without magnetic field, and at the same time, the iron contents in liver and spleen with magnetic field were lower than those without magnetic field. The results suggested that the SPION-alginate had some magnetic targeting effect *in vivo*.

In Figure 3, the ratios of iron content (right thigh/left thigh) at 0.5 and 2 h after injection were 1.17 and 1.33 without magnetic field, indicated the SPION-alginate did not be detained in injection site. On the contrary, the ratios of iron content at 0.5 and 2 h after injection were 8.88 and 7.50 with magnetic field, showed the SPION-alginate could be retained at target site with the magnetic field.

With magnetic field at 0.5 h, the femoral artery was filled with iron oxide while the femoral vein was not [Fig. 4(A)], providing a visual evidence for the magnet localization ability of SPION-alginate. Without magnetic field at 0.5 h, the iron oxide was not found

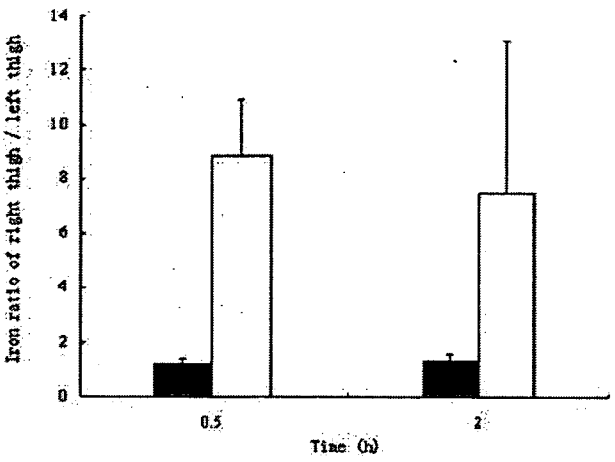

Figure 3. Iron ratio of right thigh (target site) and left thigh (nontarget site) with (□) or without (■) magnetic field at 0.5 and 2 h after injection of SPION-alginate. Data represent mean ± SD ($n = 3$).

both in femoral artery and in femoral vein [Fig. 4(B)], suggesting that no SPION-alginate was detained in the vascular system without magnetic field.

Iron oxide is well-known to significantly shorten the transverse relaxation times (T2 or T2*) with a subsequent loss of MR signal intensity.[19] Therefore, iron oxide can result in a strong decrease in signal intensity (negative enhancement) of the tissues where they accumulate. Figure 5(A) on T2*-weighted image showed the localization of the iron oxide nanoparticles at the right thigh (circle) with the magnetic field, but no localization was showed without magnetic field [Fig. 5(B)].

Hemolysis and erythrocytes aggregation analysis

The leakage of hemoglobin was used to quantify the erythrocytes damage by the SPION-alginate. As shown in Table I, the hemolysis of three preparations of SPION-alginate with different series concentrations were below 5%. So the SPION-alginate did not show hemolytic effect, that is no destruction to the red blood cell membranes. Furthermore, erythrocytes were incubated with the SPION-alginate for 1 h at 37°C, and no aggregation was observed.

Cytotoxicity analysis

The results of the MTT assay indicated that the viability of L929 and RAW264.7 apparently unaltered

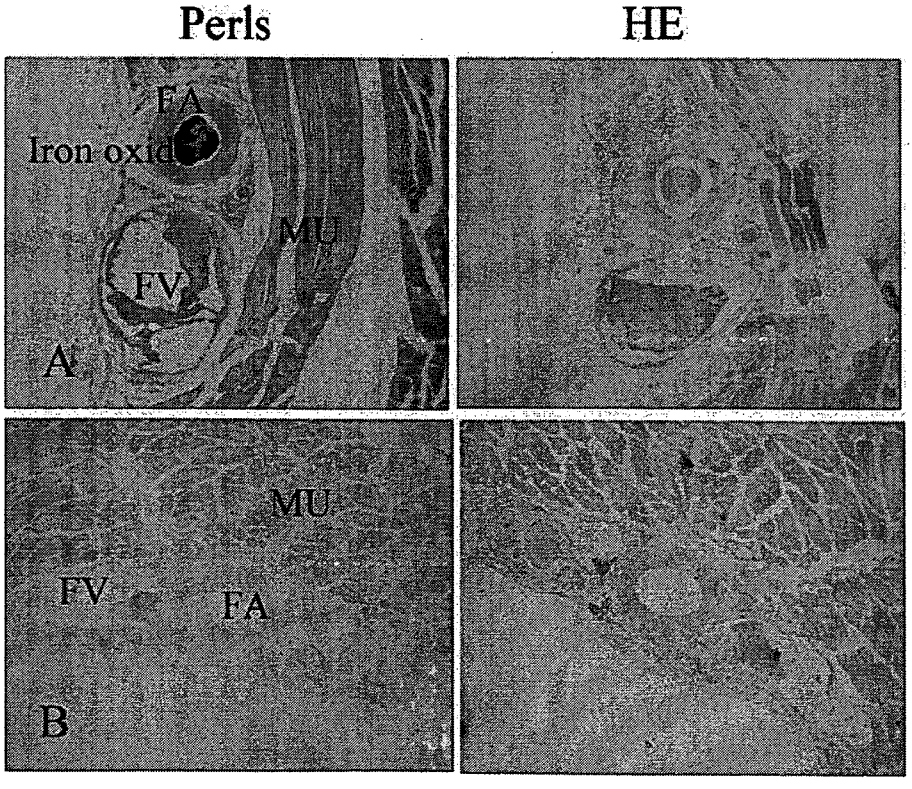

Figure 4. Micrographs of rat right thigh (target site) after femoral arterial injection with magnetic field (A) or without magnetic field (B) at 0.5 h. The tissues were stained with H&E and Perls. FA, femoral artery; FV, femoral vein; MU, muscle (×40 magnification). [Color figure can be viewed in the online issue, which is available at www.interscience.wiley.com.]

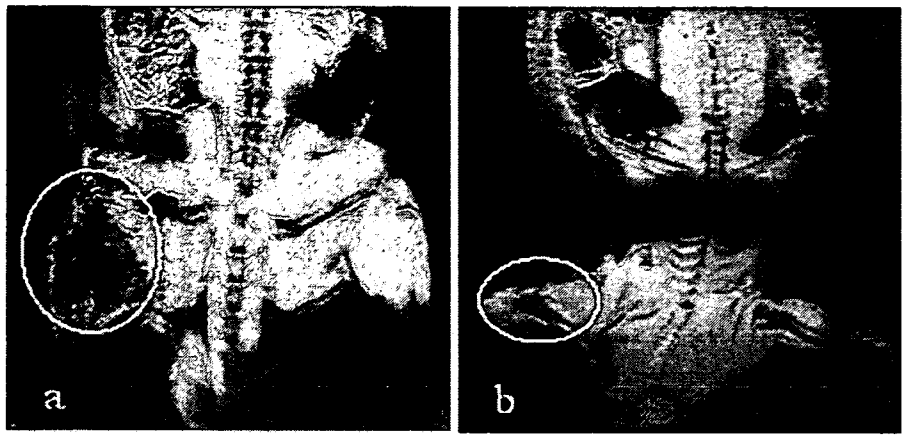

Figure 5. T2*-weighted MRI of right thigh after femoral injection of SPION-alginate with 0.5 h exposure time to magnetic field (A) or not (B). The images were taken at 10 h after injection, which still showed accumulation of iron oxide in target site with the magnetic field, since the strong signal intensity decreased (white circle in A). But the iron oxide did not accumulate in target site (white circle in B), which could be attributed to the slight change of signal intensity without the magnetic field.

upon exposure to various concentrations of SPION-alginate for 24 h with or without NCS (Fig. 6).

Cell labeling with SPION-alginate

Following 1–24 h incubation with SPION-alginate, almost all RAW264.7 cell labeling were achieved. It was evident that the labeled RAW264.7 cells contained abundant Fe_3O_4 nanoparticles in the cytoplasm after incubation with the iron concentration of 12.5, 25.0, and 50.0 μg/mL. The SPION-alginate was internalized into RAW264.7 cells in a concentration- and time- dependent manner (Fig. 7). At a concentration of 25.0 μg/mL, cells started to internalize iron particles already after 1 h incubation [Fig. 7(B)] and the internalization was increased from 1 to 24 h incubation [Fig. 7(C–E)]. For 5 h of incubation at different concentrations, it showed the amount of Prussian blue positive particles in cytoplasma as follow: 50.0 > 25.0 > 12.5 μg/mL. However, no stainable iron was detected in the control cells [Fig. 7(A)].

TABLE I
Hemolysis Percentage of Rabbit Erythrocytes at 37°C After 3 h Incubation With Different Concentrations of SPION-Alginate

SPION-Alginate Concentration (mg Fe/mL)		
Bulk Suspension	Final Suspension	Hemolysis (%)
2.08	0.04	−0.34 ± 0.16
2.08	0.08	0.71 ± 0.78
2.08	0.12	0.29 ± 0.16
2.08	0.17	1.15 ± 0.34
2.08	0.21	2.08 ± 1.48
3.62	0.07	0.23 ± 1.15
3.62	0.14	0.62 ± 1.41
3.62	0.22	1.03 ± 0.70
3.62	0.29	3.19 ± 1.56
3.62	0.36	3.19 ± 1.09
5.74	0.11	1.38 ± 0.96
5.74	0.23	0.62 ± 0.53
5.74	0.34	2.21 ± 0.89
5.74	0.46	2.35 ± 1.74
5.74	0.57	3.24 ± 0.26

Data represent mean ± SD (n = 3). The hemolysis >5% was regarded as erythrocytes hemolysis.

DISCUSSION

To optimize magnetic targeting, several factors need to be considered, (a) the magnetic field, including magnetic intensity and magnetic intensity gradient, should be of sufficient strength to attract the magnetic nanoparticles into the target site; (b) the

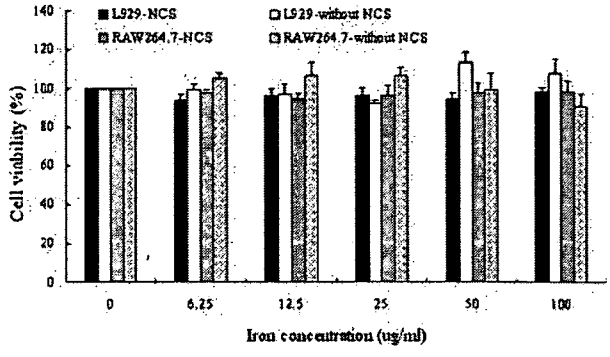

Figure 6. Viability of L929 cells and RAW264.7 cells exposed to SPION-alginate for 24 h at various iron concentrations ranging from 6.125 to 100.0 μg/mL. Cell viability is expressed as the mean ± SD of the percentage of absorbance of controls, where 100% equals viability of the control cells. The experiments were performed in hexakis and were repeated three times.

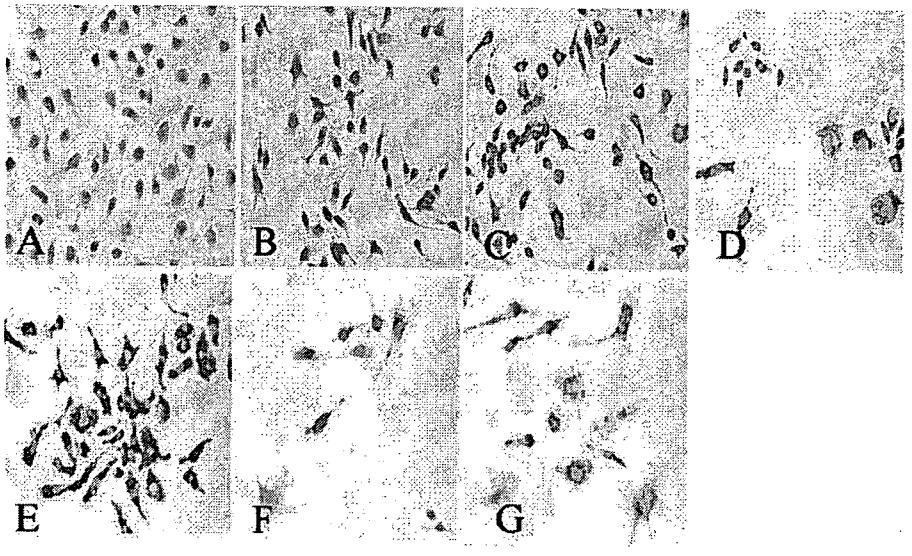

Figure 7. Photomicrographs of Prussian blue stained labeled and control RAW264.7 cells. Cells were cultured with different concentrations of SPION-alginate and harvested after different incubation times. Note the abundant iron particles in the cytoplasm of the cells (blue dots). (A) control; (B) SPION-alginate 25.0 μg/mL, 1 h; (C) SPION-alginate 25.0 μg/mL, 5 h; (D) SPION-alginate 25.0 μg/mL, 12 h; (E) SPION-alginte 25.0 μg/mL, 24 h; (F) SPION-alginate 12.5 μg/mL, 5 h; (G) SPION-alginate 50.0 μg/mL, 5 h (×400 magnification). [Color figure can be viewed in the online issue, which is available at www.interscience.wiley.com.]

magnetic particles should be of a suitable size with good magnetization and biocompatibility; (c) the method of injection should have good access to the target site and the particles should avoid clearance by RES.

In the magnetic targeting study, we employed three methods: iron content measurement, histological evaluation, and MRI. The SPION-alginate could be retained in the target site under the magnetic field with the localization ratio of 56% *in vitro* and the localization ratio of 20% *in vivo*, while reducing accumulation in the liver and spleen (Fig. 2). In addition, without magnetic field, the SPION-alginate would not be retained at the injection site (Fig. 4). The localization ratio of SPION-alginate *in vivo* was lower than that *in vitro* under the same magnetic field. One of the most important factors affecting the localization ratio of SPION-alginate *in vivo* was the rapid blood flow rate approximately 30 cm/s in large arteries.[20] Hence, part of the SPION-alginate would be flushed by the high blood flow rate which caused the decrease of the localization ratio *in vivo*. In addition, the SPION-alginate was still be phagocytosed by RES although by the artery administration.

Without magnetic field, the accumulation of SPION-alginate in liver (47.54%) and in spleen (6.66%) by femoral artery administration at 0.5 h was significantly lower than that in liver (>80%) and in spleen (10%) by vein administration at 0.5 h (data were not shown), which proved that artery injection was more advantageous than vein injection when the SPION-alginate was targeted to the sites other than liver and spleen. Furthermore, it was reported that intravenous infusion of magnetic drug particles was ineffective to make tumor remission, but the combination of artery infusion with a magnetic field was safe and effective.[2] At present, intraarterial injection of chemotherapeutic agents is approved and well accepted for treatment of liver metastases, and it has occasionally been used for other tumor types such as inoperable head and neck tumors.[21] Many other studies also confirmed the efficacy of arterial administration of magnetic targeting.[3,4,22,23] Currently, the doxorubicin hydrochloride absorbed to magnetic targeted carriers (MTC-DOX) is under clinical investigation for the treatment of patients with primary hepatocellular carcinoma (HCC). It was reported that the particles could be retained at HCC under the applied magnetic field after 28 days by intraarterial administration in human clinical trials.[21] Furthermore, a multicenter, phase I/II trial of hepatic intraarterial deliver of MTC-DOX in patients with HCC and a phase I/II dose escalation study of MTC-DOX in patients with metastatic liver tumors have been undertaken, the results indicated that MTC-DOX could be localized regionally following intraarterial administration without clinically significant toxicities in all cases.[4,23]

The magnetization of the particles was related to the magnetic field strength and the magnetic field gradient. The higher magnetic flux density and magnetic gradient it is, the better the location effect is.[2] Until now, the maximum magnetic field reported was a magnetic flux density of a maximum of 1.7

and 1.0 T at 10 mm below the tip of the pole shoe produced by electric magnet[2] and a remanence field of 1.3 T by NdFeB-permanent magnet.[24] In previous studies, it was suggested that a magnetic field strength of 0.8 T was sufficient to exceed linear blood flow in the intratumoral vasculature.[20] However, a magnetic field of only 250–1000 G has been used to locate the iron oxide particles (0.5–5 μm) in liver and lung.[25] One of the most important reasons for the great difference in strength of magnetic field used above was the difference of the magnetization of iron oxide particles. The high magnetic flux density focused onto the target area is one of the obstacles for effectively targeting. The use of larger particles, as previously suggested by Lübbe and Bergemann,[26] and the use of a stronger magnetic field, are the two approaches to overcome this problem. If the magnetization of the particle is low, a higher magnetic field is needed and vice versa. Therefore, the selection of magnetic field depends on the magnetization of the magnetic carrier. NdFeB-permanent magnet with the surface magnetic field of 3500 G and with the magnetic gradient of 2000 G/cm was used in this study. We achieved a high concentration of iron oxide within the target site after femoral artery administration of the SPION-alginate, which was seen by quantitative evaluation of iron (Figs. 2 and 3), histological (Fig. 4) and MRI (Fig. 5) methods.

As respect to the time of magnetic field added, the shortest time reported was 15 min and the longest time was 24 h.[22,24] In this study, the SPION-alginate had some magnetic targeting effect under the magnetic field at 0.5 h and as the time was prolonged to 2 h, it did not produce better magnetic target. It might be explained that the iron oxide of strong magnetism would soon be absorbed under the magnetic field of 3500 G, while those of poor magnetism would not be absorbed as the time increased and could still be phagocytosed by RES. We speculate that the time of magnetic field added depends both on the magnetization of the particles and the intensity of magnetic field. The higher magnetization of particles and the higher intensity of magnetic field, the shorter time of magnetic field.

Concerning magnetic targeting, there are many practical applications of the magnetic nanoparticles, such as magnetic drug targeting,[2–5,20,23,24] magnetic fluid hyperthermia,[6] and MRI.[9,19] The magnetic nanoparticles can act as carriers of drug and gene for site-specific drug and gene delivery. For example, the SPION-alginate can be functionalized with specific drug like chemotherapeutic drugs for chemical therapy or radioactive isotope for radionuclide therapy. Another promising application of the magnetic nanoparticles is magnetic fluid hyperthermia as one of cancer therapy strategies. When the magnetic carrier is localized at the target site with the applied magnetic field, some heat is generated under an alternating magnetic field due to magnetic hysteresis of magnetic particles. Furthermore, the magnetic nanoparticles can result in a strong decrease in MR signal intensity (negative enhancement) of the tissues where they accumulate. Therefore, it will play an important role in MR contrast imaging to better discriminate healthy and pathological tissues.

Although some encouraging data were achieved in this study, there are many issues to be further investigated on magnetic targeting. For example, a potential complication that could arise with the use of ferrofluid is the fact that an embolization process could occur after magnetic targeting, and the embolization is to some extent favorable for cancer treatment because of their cut-off of the blood and nutrition of tumor.[8] However, it was reported that the therapeutic effect resulted from the action of the chemotherapeutic agent itself, rather than intratumoral embolization by the particles.[2] On the other hand, the localization accuracy of the particles at the target site needs to be optimized, and the design of the magnetic field with greater magnetic field intensity and magnetic field gradient is quite important and needs to be improved.

Compared with the corresponding control cells, no significant change was observed in the viability of RAW264.7 cells and L929 cells with various different concentrations of SPION-alginate for 24 h incubation with or without serum (Fig. 6). Hence, we considered that the SPION-alginate was not toxic to RAW264.7 cells and L929 cells. In addition, the SPION-alginate did not induce erythrocytes hemolysis and erythrocytes aggregation. Accordingly, the SPION-alginate was generally considered to be of good biocompatibility.

Figure 7 showed that the labeled RAW264.7 cells contained abundant Fe_3O_4 nanoparticles in the cytoplasm after 1–24 h incubation with the various concentrations of SPION-alginate. The high RAW264.7 labeling efficiency with the SPION-alginate seems to be related firstly to the nonspecific process of nanoparticles adsorption on the cell membrane in the form of clusters, secondly to their subsequent internalization into endosomes, as introduced by other authors.[14,27] The interaction of the SPION-alginate with living cells should be further investigated. Moreover, the Fe_3O_4 nanoparticles bound to alginate macromolecule strands like "fruit" in the "tree," not simply coated by the polymer. They were visually confirmed by atomic force microscopy.[10] It is indicated that alginate would not hamper their interactions with cell membrane, which could be caused by steric coating effect. Besides, the good bioadhesion property of alginate is beneficial to the adsorption of SPION-alginate on the cell membrane. Because of the nonspecific cellular uptake mediated by adsorptive

endocytosis, the SPION-alginate labeling may be nonspecific and potentially applicable to a wide variety of cells, making it useful for cellular imaging strategies.

CONCLUSIONS

With magnetic field, the SPION-alginate had a localization ratio of 56% *in vitro* and 20% *in vivo*, meanwhile, the contents of the SPION-alginate in liver and spleen were reduced. The magnetic targeting effect was established by evaluating the iron content ratio of target site/nontarget site, and was visually confirmed by histological evaluation and MRI. Furthermore, the SPION-alginate was considered to be biocompatible in respects of cytotoxicity and hemolysis.

References

1. Häfeli UO. Magnetically modulated therapeutic systems. Int J Pharm 2004;277:19–24.
2. Alexiou C, Arnold W, Klein RJ, Parak FG, Hulin P, Bergemann C, Erhardt W, Wagenpfeil S, Lübbe AS. Locoregional cancer treatment with magnetic drug targeting. Cancer Res 2000;60:6641–6648.
3. Leakakos T, Ji C, Lawson G, Peterson C, Goodwin S. Intravesical administration of doxorubicin to swine bladder using magnetically targeted carriers. Cancer Chemother Pharmacol 2003;51:445–450.
4. Just R, Hoh C, Vogl T, Neese P, Doemeny J, Schechter M, Varney R, Stanton W, Schiemann M, Goldfarb P. A phase I/II single arm trial to determine the safety, tolerability, and biological activity of intrahepatic delivery of doxorubicin hydrochloride adsorbed to magnetic targeted carriers (MTX-DOX) in patients with metastatic tumors in the liver. Eur J Cancer Suppl 2003;1:S292–S293.
5. Häfeli U, Pauer G, Failing S, Tapolsky G. Radiolabeling of magnetic particles with rhenium-188 for cancer therapy. J Magn Magn Mater 2001;225:73–78.
6. Jordan A, Scholz R, Maier-Hauff K, Johannsen M, Wust P, Nadobny J, Schirra H, Schmidt H, Deger S, Loening S, Lanksch W, Felix R. Presentation of a new magnetic field therapy system for the treatment of human solid tumors with magnetic fluid hyperthermia. J Magn Magn Mater 2001;225:118–126.
7. Scherer F, Anton M, Schillinger U, Henke J, Bergemann C, Krüger A, Gänsbacher B, Plank C. Magnetofection: Enhancing and targeting gene delivery by magnetic force in vitro and in vivo. Gene Ther 2002;9:102–109.
8. Widder KJ, Senyel AE, Scarpelli GD. Magnetic microspheres: A model system for site specific drug delivery in vivo. Proc Soc Exp Biol Med 1978;158:141–146.
9. Wang YX, Hussain SM, Krestin GP. Superparamagnetic iron oxide contrast agents: Physicochemical characteristics and applications in MR imaging. Eur Radiol 2001;11:2319–2331.
10. Ma HL, Qi XR, Maitani Y, Nagai T. Preparation and characterization of superparamagnetic iron oxide nanoparticles stabilized by alginate. Int J Pharm 2007;333:177–186.
11. Sgouras D, Duncan R. Methods for the evaluation of biocompatibility of soluble synthetic polymers which have potential for biomedical use: 1-Use of the tetrazolium-based colorimetric assay (MTT) as a preliminary screen for evaluation of in vitro cytotoxicity. J Mater Sci: Mater Med 1990;1:61–68.
12. Biological Evaluation for Medical Devices, Part 5: Tests for Cytotoxicity: In Vitro Methods. United States Pharmacopeia XXIII, 1995.
13. Biological Evaluation of Medical Devices, Part 5: Test for In Vitro Cytotoxicity. ISO 10993-5 (EN 30993-5), 1999.
14. Wilhelm C, Billotey C, Roger J, Pons JN, Bacri JC, Gazeau F. Intracellular uptake of anionic superparamagnetic nanoparticles as a function of their surface coating. Biomaterials 2003;24:1001–1011.
15. Hagar W, Vichinsky EP, Theil EC. Liver ferritin subunit ratios in neonatal hemochromatosis. Pediatr Hematol Oncol 2003;20:229–235.
16. Regulations of new drug license application in China.State Food and Drug Administration in China; 1999. p 24.
17. Mosmann T. Rapid colorimetric assay for cellular growth and survival: Application to proliferation and cytotoxicity assays. J Immunol Methods 1983;65:55–63.
18. Arbab AS, Bashaw LA, Miller BR, Jordan EK, Lewis BK, Kalish H, Frank JA. Characterization of biophysical and metabolic properties of cells labeled with superparamagnetic iron oxide nanoparticles and transfection agent for cellular MR imaging. Radiology 2003;229:838–846.
19. Saini S, Stark DD, Hahn PF, Wittenberg J, Brady TJ, Ferrucci JT. Ferrite particles: A superparamagnetic MR contrast agent for the reticuloendothelial system. Radiology 1987;162:211–216.
20. Senyei A, Widder K, Czerlinski C. Magnetic guidance of drug carrying microspheres. J Appl Phys 1978;49:3578–3583.
21. Link KH, Kornmann M, Formenti A, Leder G, Sunelaitis E, Schatz M, Pressmar J, Beger HG. Regional chemotherapy of non-resectable liver metastases from colorectal cancer-literature and institutional review. Langenbecks Arch Surg 1999;384:344–353.
22. Rudge S, Peterson C, Vessely C, Koda J, Stevens S, Catterall L. Adsorption and desorption of chemotherapeutic drugs from a magnetically targeted carrier (MTC). J Control Release 2001;74:335–340.
23. Koda J, Venook A, Walser E, Goodwin S. A multicenter, phase I/II trial of hepatic intra-arterial delivery of doxorubicin hydrochloride adsorbed to magnetic targeted carriers in patients with hepatocellular carcinoma. Eur J Cancer 2002;38(Suppl 7):S18.
24. Schulze K, Koch A, Schöpf B, Petri A, Steitz B, Chastellain M, Hofmann M, Hofmann H, von Rechenberg B. Intraarticular application of superparamagnetic nanoparticles and their uptake by synovial membrane—An experimental study in sheep. J Magn Mag Mater 2005;293:419–432.
25. Goodwin S, Peterson C, Hoh C, Bittner C. Targeting and retention of magnetic targeted carriers (MTCs) enhancing intra-arterial chemotherapy. J Magn Mag Mater 1999;194:132–139.
26. Lübbe AS, Bergemann C.Selected preclinical and first clinical experiences with magnetically targeted 4′-epidoxorubicin in patients with advanced solid tumors. In: Häfeli U, Schütt W, Teller J, Zborowski M, editors. Scientific and Clinical Application of Magnetic Carriers. New York:Plenum; 1997. p 457–480.
27. Wilhelm C, Gazeau F, Roger J, Pons JN, Bacri JC. Interaction of anionic superparamagnetic nanoparticles with cells: Kinetic analyses of membrane adsorption and subsequent internalization. Langmuir 2002;18:8148–8155.

Available online at www.sciencedirect.com
ScienceDirect
ELSEVIER
International Journal of Pharmaceutics xxx (2007) xxx–xxx
INTERNATIONAL JOURNAL OF PHARMACEUTICS
www.elsevier.com/locate/ijpharm

Pharmaceutical nanotechnology

Hydroxyethylated cationic cholesterol derivatives in liposome vectors promote gene expression in the lung

Wuxiao Ding [a], Yoshiyuki Hattori [a], Kimio Higashiyama [b], Yoshie Maitani [a,*]

[a] *Fine Drug Targeting Research Laboratory, Institute of Medicinal Chemistry, Hoshi University, Ebara 2-4-41, Shinagawa-ku, Tokyo 142-8501, Japan*
[b] *Synthetic Organic Chemistry Research Laboratory, Institute of Medicinal Chemistry, Hoshi University, Ebara 2-4-41, Shinagawa-ku, Tokyo 142-8501, Japan*

Received 25 July 2007; received in revised form 27 September 2007; accepted 21 October 2007

Abstract

Three cationic cholesterol derivatives (CCDs), which differ in their types of amine and bear a hydroxyethyl group at the amine group, were synthesized and formulated into liposomes and nanoparticles as gene delivery vectors. *In vitro* transfection into A549 cells proved that liposomes formulated with CCDs and dioleoylphosphatidylethanolamine (DOPE) of 1/2 molar ratio were more effective than the corresponding nanoparticles with CCDs and Tween 80 at charge ratios (+/−) of 1/2, 3/1 and 5/1. Among the liposomal formulations, non-hydroxyethylated CCDs were more effective than hydroxyethylated ones *in vitro*. However, gene transfection in the lung through intratracheal injection showed opposite results to those *in vitro*, with liposomes containing hydroxyethylated CCDs being more potent than those containing non-hydroxyethylated CCDs. Transfection by liposomes with *N,N*-methyl hydroxyethyl aminopropane carbamoyl cholesterol iodide (MHAPC) showed the highest luciferase activity, resulting in 2- and 60-fold higher gene expression than jet-PEI and naked DNA, respectively. The distribution of MHAPC lipoplex after intratracheal injection was heterogeneous, and luciferase was expressed in epithelial cells lining the bronchi and bronchioles. All the lipoplexes led to higher TNF-α levels in the lung compared to the nanoplex and jet-PEI, but our findings suggested that modification of the cationic cholesterol with a hydroxyethyl group at the tertiary amine terminal, MHAPC, promoted gene expression in the lung without increasing the toxicity compared with other CCDs. This work firstly proved that liposomes containing hydroxyethylated CCDs could promote gene expression in the lung through intratracheal injection.

Keywords: Cationic liposomes; Nanoparticles; Intratracheal injection; Cationic cholesterol derivatives; Hydroxyethyl group

1. Introduction

Gene therapy in the lung still holds promise as an effective method for treating cystic fibrosis and lung neoplastic disease (Hoag, 2005). Gene delivery vectors are classified into viral and non-viral ones, and both of them have been well studied. Cationic lipids (Miller, 2003) and polymers (Pietersz et al., 2006), which can compact negatively charged genetic materials through electrostatic interaction and transport them into the cells, constitute a large fraction of non-viral vectors. Many cationic lipids have been reported to mediate gene delivery *in vitro* and *in vivo* (Miller, 2003), and more are being reported all the time.

After the discovery of 3β-[*N*-(*N*′,*N*′-dimethylaminoethane) carbamoyl] cholesterol (DC-Chol) (Gao and Huang, 1991), many effective cationic cholesterol derivatives (CCDs) were soon developed (Ghosh et al., 2002; Hasegawa et al., 2002; Miller, 2003; Nakanishi, 2003; Percot et al., 2004; Bajaj et al., 2007). CCDs are amphiphilic molecules that consist of a cationic headgroup attached via a linker to the cholesteryl skeleton. Clearly, the linker and the cationic headgroup are crucial for the gene transfection ability and toxicity. The inability of CCD-containing cationic liposomes to produce persistent gene expression (Scheule et al., 1997) results in a need for repeated dosing of the liposomes. Therefore, biodegradable CCDs with a linker such as carbamate ester, which can facilitate degradation *in vivo*, are strongly recommended for the design and synthesis of CCDs (Choi et al., 2001). In fact, this strategy has already been verified to be effective by the low toxicity of DC-Chol (Gao and Huang,

* Corresponding author. Tel.: +81 3 5498 5048; fax: +81 3 5498 5048.
E-mail address: yoshie@hoshi.ac.jp (Y. Maitani).

0378-5173/$ – see front matter © 2007 Elsevier B.V. All rights reserved.
doi:10.1016/j.ijpharm.2007.10.051

1991) and cationic 3β-[L-lysinamide-carbamoyl]cholesterol derivatives (K-Chol) (Choi et al., 2001; Lee et al., 2006).

Moreover, the amine headgroups of cationic lipids definitely determine their transfection ability (Reynier et al., 2004). Among various amine headgroups, hydroxyethyl group-containing ones have exhibited higher gene transfection than the corresponding hydroxyethyl-lacking ones (Okayama et al., 1997; Venkata Srilakshmi et al., 2002; Arpicco et al., 2004). Cholesteryl-3β-carboxyaminoethylene-*N*-hydroxyethylamine (OH-Chol) is a cationic cholesterol with a hydroxyethyl group at the amine headgroup, linked to the cholesteryl skeleton by an amido bond. Liposomes containing OH-Chol and phosphatidylethanolamine (DOPE) showed high gene transfection ability (Okayama et al., 1997). Furthermore, a nanoparticle formulation with OH-Chol exhibited excellent gene transfection. Their high gene transfection activity was ascribed to the hydroxyethyl group at the cationic headgroup of OH-Chol (Hattori et al., 2007). The combination of a hydroxyethyl group at the headgroup and amine lipids, therefore, will produce effective cationic carbamate-linked lipids for gene delivery vectors.

To develop highly potent and biodegradable CCDs, in this study, we synthesized three types of CCDs bearing secondary, tertiary and quaternary amines, with a carbamate ester linker and a hydroxyethyl group at the amine headgroup. The synthesized CCDs were formulated into nanoparticles and liposomes, and their formulations were optimized for gene transfection of the human lung adenocarcinoma A549 cell line and into the mouse lung through intratracheal injection. The location of luciferase expression was studied by immunohistochemistry. Furthermore, the inflammatory response of the nanoplexes and lipoplexes was evaluated.

2. Materials and methods

2.1. Materials and instrumentation

DC-Chol and cholesterol chloroformate were purchased from Sigma–Aldrich (St. Louis, USA). *N,N*-Dimethyl-1,3-propanediamine; *N*-methyl-1,3-propanediamine; 1,3-propanediamine; 2-iodoethanol were purchased from Wako Pure Chemistry (Osaka, Japan). Tween 80 was obtained from NOF Co. Ltd. (Tokyo, Japan) and DOPE was from Avanti Polar Lipids Inc., (Alabaster, AL, USA). The synthesis of OH-Chol was done as previously reported (Hattori et al., 2005). RPMI-1640 culture medium was purchased from Invitrogen Corp. (Carlsbad, CA, USA). ^{1}H NMR (270 MHz) and ^{13}C NMR (67.8 MHz) spectra were recorded using tetramethylsilane as an internal standard with a JEOL JNM-LA270 spectrometer. Chemical ionization (CI) was carried out on JEOL JMS 600 (JEOL, Tokyo, Japan). The plasmid pCMV-luc encoding the luciferase gene under the control of the CMV promoter was constructed as previously described (Igarashi et al., 2006). A protein-free preparation of the plasmid was purified following alkaline lysis using Maxiprep columns (Qiagen, Hilden, Germany).

2.2. Synthesis of cationic cholesterol derivatives (Fig. 1)

2.2.1. N,N,N-Dimethyl aminopropane carbamoyl cholesterol iodide (DMAPC, 1) and N,N,N-dimethyl hydroxyethyl aminopropane carbamoyl cholesterol iodide (DMHAPC, 2)

1 was synthesized as described by Percot et al. (2004) and hydroxyethylated to **2** with some modifications. **1** and iodoethanol were refluxed in toluene (with a catalytic amount of DMF) at 105 °C for 24 h. Silica-gel chromatography with $CHCl_3$/methanol for elution gave **2** (yield 70%), a pale yellow powder.

2.2.2. N-Hydroxyethyl aminopropane carbamoyl cholesterol iodide (HAPC, 3)

A solution of cholesterol chloroformate (2.7 g, 6 mmol) in 10 ml of dry dichloride methylene (DCM) was slowly added to a pre-cooled solution of 1,3-propanediamine (5 ml, 60 mmol) in 100 ml of DCM. The mixture was further stirred at RT for 1 h. After the reaction, the solvent was removed by vacuum evaporator and the residue was purified on silica gel to give aminopropane carbamoyl cholesterol (2.8 g, 95%). 2.8 g (5.75 mmol) of aminopropane carbamoyl cholesterol was dissolved in a mixture of DCM/methanol with 1 equiv. of triethylamine, and iodoethanol (1.9 mmol, 150 μl) was added and

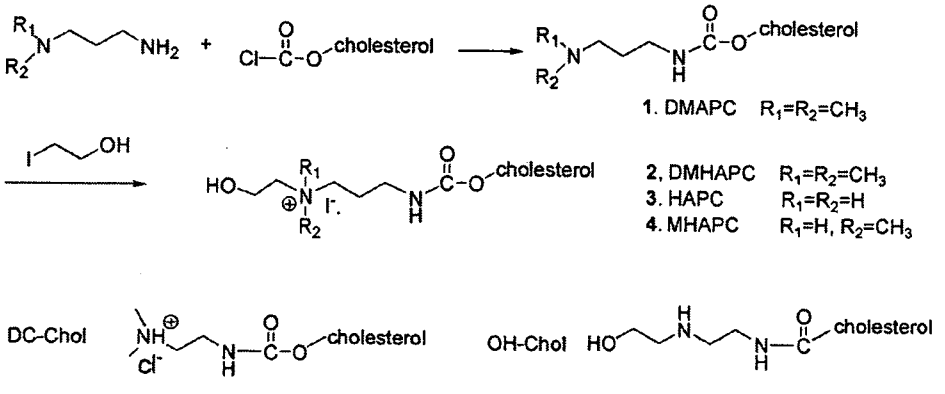

Fig. 1. Chemical structures and synthesis of cationic cholesterol derivatives.

stirred at RT for 24 h. Careful purification on silica-gel chromatography with $CHCl_3$/methanol for elution gave **3** (1.2 g, 31%). ^1H NMR ($CDCl_3$) δ: 7.62 (s, 1H, –CO–NH–C), 5.36 (t, 3H, C=CH–C), 4.41 (m, 1H, CH–O–CO–), 4.1 (m, 2H, –C–CH_2–O). ^{13}C NMR ($CDCl_3$) δ: 157.2 (NH–CO–O), 139.5, 122.5 (C=CH), 74.9 (=CH–O), 64.9 (–CH_2–OH). CI-MS *m/z*: found 658 (Calcd for $C_{33}H_{59}IN_2O_3$, 658.36).

2.2.3. *N,N-Methyl hydroxyethyl aminopropane carbamoyl cholesterol iodide (MHAPC, 4)*

Similarly to **3**, **4** (3.6 g, 94%) was synthesized from *N*-methyl-propanediamine (3.7 ml, 30 mmol) and cholesterol chloroformate (2.7 g, 6 mmol) and subsequently hydroxyethylated with iodoethanol (6.84 mmol, 540 μl). ^1H NMR ($CDCl_3$) δ: 7.91 (s, 1H, –CO–NH–C), 5.36 (t, 3H, C=CH–C), 4.41 (m, 1H, CH–O–CO–), 4.1 (m, 2H, –C–CH_2–O), 2.92 (s, 3H, CH_3–N^+). ^{13}C NMR ($CDCl_3$) δ: 158.1 (NH–CO–O), 139.2, 122.8 (C=CH), 74.8 (=CH–O), 63.2 (–CH_2–OH). CI-MS *m/z*: found 673 (Calcd for $C_{34}H_{61}IN_2O_3$, 672.37).

2.3. *Preparation of liposomes/lipoplexes and nanoparticles/nanoplexes*

The synthesized CCDs, namely DMAPC, DMHAPC, HAPC and MHAPC, together with DC-Chol and OH-Chol (Fig. 1), were formulated into liposomes with DOPE and into nanoparticles with 5% Tween 80 by a modified ethanol injection method (Hattori et al., 2005). The molar ratio of CCDs to DOPE in the liposomes was varied from 2/1 to 1/1 to 1/2. Each type of liposomes and nanoparticles contained 0.9 mM CCD lipid concentration for *in vitro* transfection and 4.5 mM for *in vivo* experiments.

The CCD liposome/DNA complex (CCD lipoplex) and CCD nanoparticle/DNA complex (CCD nanoplex) for *in vitro* transfection at various charge ratios (+/−) of CCD to DNA were prepared by addition of each liposome or nanoparticle preparations (1.67, 10, 16.7 μl for the charge ratio (+/−) of 1/2, 3/1 and 5/1) to 1 μg of DNA in 5 μl of MilliQ water with 10 rounds of pipetting. After the preparations were left at room temperature for 15 min, the size of each lipoplex/nanoplex in water was measured after incubation with RPMI-1640 medium for a further 15 min. The mean particle size was measured by the dynamic light scanning method (ELS-Z2, Otsuka Electronics Co. Ltd., Osaka, Japan). For the *in vivo* study, the lipoplexes and nanoplexes at charge ratio (+/−) of 3/1 were prepared by the addition of 40 μl of liposomes or nanoparticles, respectively to 20 μg of DNA in 25 μl of MilliQ water. The total injection volume was fixed at 65 μl per mouse.

2.4. *Cell culture*

The human lung adenocarcinoma A549 cell line was kindly provided by OncoTherapy Science, Inc. (Kanagawa, Japan). The cells were maintained in RPMI-1640 medium supplemented with 10% FBS and kanamycin (100 μg/ml) at 37 °C in a 5% CO_2 humidified incubator.

2.5. *Gene transfection in A549 cell line and in the lung*

For transfection into A549 cells, the lipoplexes or nanoplexes were diluted in 500 μl of 10% FBS supplemented RPMI-1640 and then incubated with the cells in 12-well plates for 24 h. As a positive control, the Lipofectamine 2000 (LA2000, Invitrogen Corp.)/DNA complex was prepared according to the manufacturer's protocol.

To study the gene expression in the mouse lung, intratracheal injection through the exposed trachea was used as an injection method. Briefly, a ddY mouse (male, 5 weeks of age, Sankyo Lab., Shizuoka, Japan) was anesthetized with phenobarbital sodium (50 μg/g body weight) by intraperitoneal injection (i.p.). Then the mouse was positioned in a vertical position and the trachea was exposed by blunt dissection of the neck. Sixty-five microliters of complex suspension per mouse was bolus injected into the trachea using a 29G injection syringe. The jet-PEI (polyplus-transfection, NY, USA)/DNA complex was prepared at a (+/−) ratio of 5/1 according to the manufacturer's instructions.

2.6. *Luciferase assay and TNF-α in the lung tissue*

Luciferase expression in A549 cells was measured as counts per second (cps)/μg total protein using the luciferase assay system (Picagene, Tokyo Ink Mfg. Co. Ltd., Tokyo, Japan) and BCA reagent (Pierce, IL, USA) as previously described (Maitani et al., 2007).

The luciferase in the lung was measured 24 h after intratracheal injection. Mice were anesthetized with ethyl ether and the lung was perfused with 10 ml of PBS through the left ventricle to remove the blood. The lung was collected with minimal main bronchi and immediately homogenized in 500 μl of cold lysis buffer (Promega Co., Madison, WI, USA). The homogenate samples were centrifugated at 15,000 rpm for 5 min at 4 °C and the luciferase assay was done as described above.

For TNF-α measurement, lysates were prepared exactly as described for the luciferase assay in the lung. TNF-α levels were determined using a mouse TNF-α ELISA kit (R&D, Minneapolis, MN, USA).

2.7. *Immunohistochemistry of luciferase in the lung*

0.01% (molar percentage of lipids) rhodamine-DHPE (*N*-(lissamine rhodamine B sulfonyl)-1,2-dihexadecanoyl-*sn*-glycero-3-phosphoethanolamine, triethylammonium salt) labeled MHAPC liposomes (MHAPC/DOPE=1/2, molar ratio) were prepared with MHAPC concentration of 4.5 mM as described in Section 2.3. The lipoplex was prepared with 20 μg of DNA at a charge ratio (+/−) of 3/1. The lipoplexes were intratracheally injected into mouse lung, and the lung was collected at 24 h. The frozen lungs were cryosectioned into 12 μm slices. The sections were fixed with 70% ethanol and washed in PBS before incubation with primary goat anti-luciferase pAb (1:100) (Promega Co.). The sections were then incubated in bovine serum albumin (BSA) to reduce non-specific binding of a secondary antibody. Finally, they were incubated with rabbit

Please cite this article in press as: Ding, W., et al., Hydroxyethylated cationic cholesterol derivatives in liposome vectors promote gene expression in the lung, Int J Pharm (2007), doi:10.1016/j.ijpharm.2007.10.051

anti-goat IgG–HRP (Santa Cruz Biotech, Santa Cruz, CA, USA) for 2 h. The color was developed using a peroxidase substrate kit DAB SK-400 (Vector Lab, Inc. Burlingame, CA, USA).

3. Results and discussion

3.1. DOPE content in liposomes affected gene transfection

DOPE played a very important role in the destabilization of liposomes upon contact with cellular membranes and/or endosomes. In the formulations of cationic liposomes containing DOPE as a helper lipid, most studies used cationic lipids/DOPE at a molar ratio of 2/1, 3/2 or 1/1 as the optimum formulation (Miller, 2003). Recently we reported that DC-Chol/DOPE (1/2, molar ratio) liposomes, which were prepared by a modified ethanol injection method, were more effective for gene transfection than DC-Chol/DOPE = 1/1 and 3/2 liposomes (Maitani et al., 2007). To optimize the CCD liposomes, therefore, at first the DOPE content in liposomes was investigated in an attempt to determine the most effective formulations. As shown in Fig. 2, all the lipoplexes showed higher gene transfection in A549 cells with increasing molar ratio of DOPE (CCD/DOPE = 1/2, molar ratio) at a charge ratio (+/−) of 3/1, lipoplexes with less DOPE content (CCD/DOPE = 1/1 and CCD/DOPE = 2/1) were not effective enough to transfect A549 cells. Therefore, a liposome formulation rich in DOPE content, CCD/DOPE = 1/2-liposomes, was used for further studies. The lipoplexes were named DC-Chol, DMAPC, DMHAPC, HAPC and MHAPC lipoplexes.

3.2. Characterization of lipoplexes and nanoplexes

Although liposomes rich in DOPE had higher gene transfection ability than those poor in DOPE, they were only 1/10 to 1/50 as effective as LA-2000 (Fig. 2). Since a nanoparticle formulation with OH-Chol and Tween 80 has shown excellent gene transfection (Hattori et al., 2007), we prepared CCD nanoparticles using Tween 80 as well as CCD liposomes and investigated their use for gene transfection in A549 cells at three charge ratios (+/−) of 1/1, 3/1 and 5/1.

The liposomes and nanoparticles prepared by modified ethanol injection had a mean particle size of about 200 nm, with zeta-potential from +40 to +60 mV, except for OH-Chol/DOPE (1/2, molar ratio) liposomes, which were about 400 nm in size.

To establish the relationship between gene transfection and particle size, the size of lipoplexes (Fig. 3A) and nanoplexes (Fig. 3B) was measured after incubation with RPMI-1640 culture medium. CCD lipoplexes or nanoplexes showed a mean

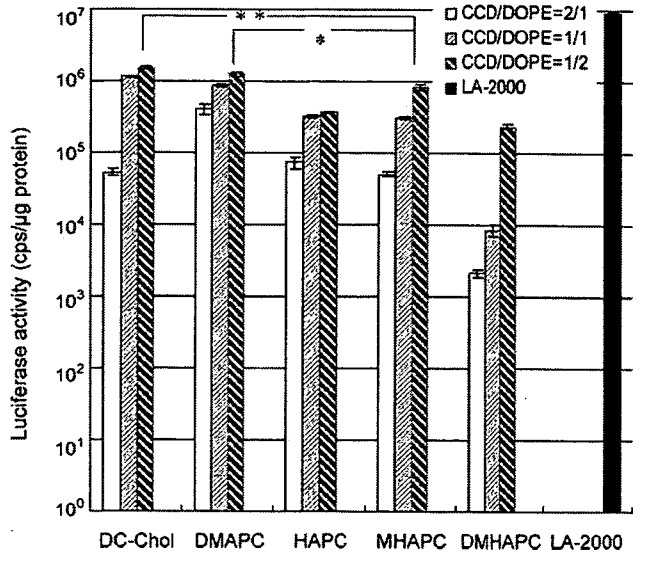

Fig. 2. Effect of DOPE composition in CCD lipoplexes on transfection efficiencies. LA-2000 is lipofectamine-2000. Charge ratio (+/−) was 3/1 and the amount of DNA was 1 μg/well. The values are expressed as mean ± S.D. ($n = 3$). *$P < 0.05$, **$P < 0.01$, Student's t test.

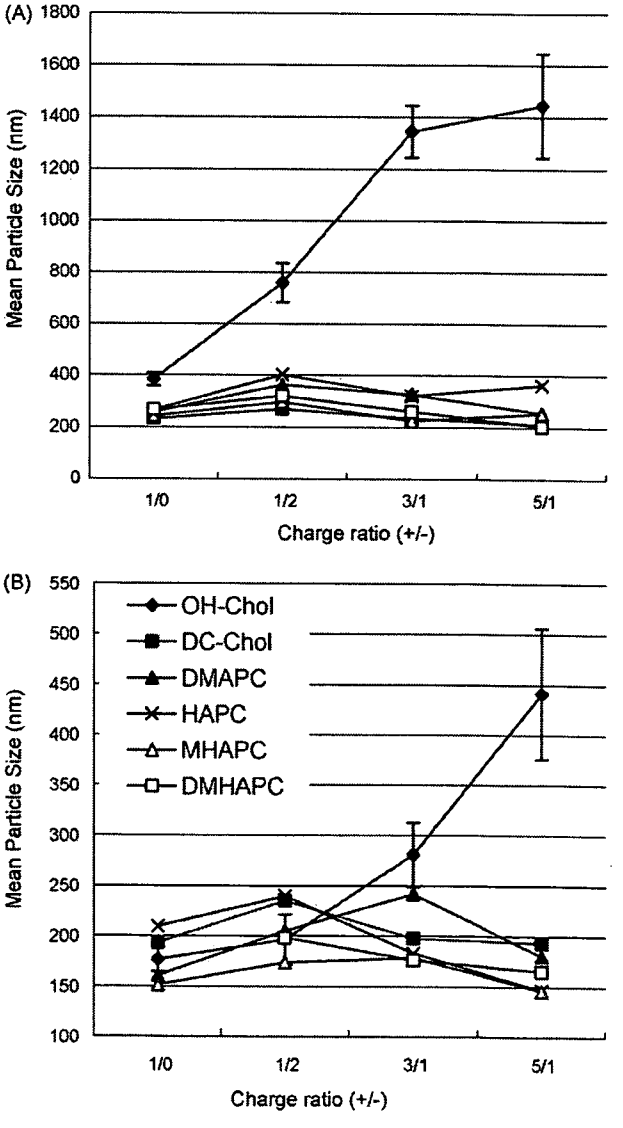

Fig. 3. Particle size of lipoplexes (A) and nanoplexes (B) after incubation with RPMI-1640 medium. The size of each lipoplex and nanoplex in water was measured after incubation with RPMI-1640 medium for 15 min. The values for OH-Chol were expressed as mean ± S.D., other values are expressed as mean values ($n = 3$).